ARTICLE IN PRESS – J. Synchrotron Rad



A MHz X-ray diffraction set-up for dynamic compression experiments in the diamond anvil cell

ISSN 1600-5775

Proof instructions

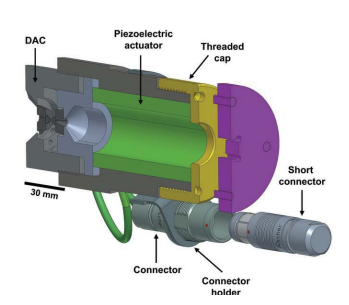
Proof corrections should be returned by 28 May 2023. After this period, the Editors reserve the right to publish your article with only the Managing Editor's corrections.

Please

- (1) Read these proofs and assess whether any corrections are necessary.
- (2) Check that any technical editing queries highlighted in **bold underlined** text have been answered.
- (3) Send corrections by e-mail to **tw@iucr.org**. Please describe corrections using plain text, where possible, giving the line numbers indicated in the proof. Please do not make corrections to the pdf file electronically and please do not return the pdf file. If no corrections are required please let us know.

To purchase printed offprints, please complete the attached order form and return it by e-mail.

Please check the following details for your article



Thumbnail image for contents page

Synopsis: A MHz X-ray diffraction set-up for the investigation of material behaviour under dynamic compression in the diamond anvil cell at intermediate strain rates has been developed at the High Energy Density (HED) instrument at the European XFEL.

Abbreviated author list: Husband, R.J.; Strohm, C.; Appel, K. (10 0000-0002-2902-2102); Ball, O.B.; Briggs, R. (D 0000-0003-4588-5802); Buchen, J. (D 0000-0001-5671-5214); Cerantola, V. (D 0000-0002-2808-2963); Chariton, S. (D 0000-0001-5522-0498); Coleman, A.L. (D 0000-0002-5692-4400); Cynn, H.; Dattelbaum, D.; Dwivedi, A.; Eggert, J.H.; Ehm, L. (10 0000-0001-5485-0316); Evans, W.J.; Glazyrin, K. (10 0000-0002-5296-9265); Goncharov, A.F. (10 0000-0002-6422-8819); Graafsma, H. (10 0000-0003-2304-667X); Howard, A. (10 0000-0003-2358-8997); Huston, L.; Hutchinson, T.; Hwang, H.; Jacob, S. (10 0000-0003-2859-3437); Kaa, J. (10 0000-0003-3862-4911); Kim, J. (10 0000-0003-1787-3775); Kim, M.; Koemets, E.; Konôpková, Z.; Langenhorst, F. (10 0000-0003-4892-7713); Laurus, T. (10 0000-0002-2258-2123); Li, X.; Mainberger, J. (60000-0001-6591-7037); Marquardt, H.; McBride, E.E. (600000-0002-8821-6126);

McGuire, C.; McHardy, J.D. (🕞 0000-0002-2630-8092); McMahon, M.I.; McWilliams, R.S.; Méndez, A.S.J.; Mondal, A. (🕞 0000-0002-3424-0001-9270-2330); Prescher, C. (📵 0000-0002-9556-1032); Preston, T.R. (📵 0000-0003-1228-2263); Redmer, R. (📵 0000-0003-3440-863X); Roeper, M.; Sanchez-Valle, C.; Smith, D. (6) 0000-0001-5491-747X); Smith, R.F.; Sneed, D.; Speziale, S.; Spitzbart, T.; Stern, S.; Sturtevant, B.T. (10 0000-0002-9934-6508); Sztuk-Dambietz, J.; Talkovski, P.; Velisavljevic, N.

Keywords: extreme conditions science; X-ray free-electron lasers; diamond anvil cells; dynamic compression

How to cite your article in press

Your article has not yet been assigned page numbers, but may be cited using the doi:

Husband, R.J., Strohm, C., Appel, K., Ball, O.B., Briggs, R., Buchen, J., Cerantola, V., Chariton, S., Coleman, A.L., Cynn, H. et al. (2023). J. Synchrotron Rad. 30, https://doi.org/10.1107/S1600577523003910.

You will be sent the full citation when your article is published and also given instructions on how to download an electronic reprint of your article.

59

60

61

62

63

65

67

69

70

71

72

73

74

75

76

77

78

79

80

82

83

84

86

88

89

90

91

92

93

94

95

96

97

98

99

100

102

103

104

105

106

107

108

109

110

111

112

113

114

42

46

50

51

52

53

54

55

56

57



JOURNAL OF SYNCHROTRON RADIATION

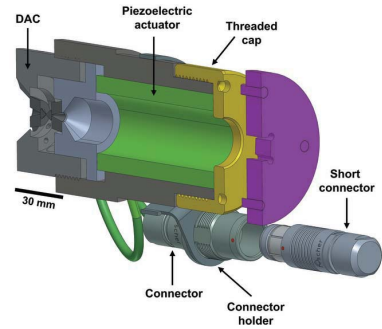
ISSN 1600-5775

Received 22 February 2023 Accepted 2 May 2023

Edited by V. Favre-Nicolin, ESRF and Université Grenoble Alpes, France

- ‡ Current address: Department of Earth and Environmental Sciences (DISAT), University of Milano-Bicocca, Piazza della Scienza 4, 20126 Milan, Italy.
- § Current address: School of Earth Sciences and Environmental Engineering, Gwangju Institute of Science and Technology, 123 Cheomdan-Gwagiro, Gwangju 61005, Republic of Korea. ¶ Current address: College of Physics,
- State Key Laboratory of Superhard Materials, Jilin University, Changchun 130012, China. ## Current address: Queen's University Belfast, School of Mathematics and Physics, University Road, Belfast BT7 1NN, UK
- §§ Current address: University of Nevada, Las Vegas, Nevada Extreme Conditions Laboratory, 4505 S. Maryland Pkwy, Las Vegas, NV 89154,
- ¶¶ Current address: X-Spectrum GmbH, Luruper Hauptstraße 1, 22547 Hamburg, Germany.

Keywords: extreme conditions science; X-ray free-electron lasers; diamond anvil cells; dynamic compression





Published under a CC BY 4.0 licence

A MHz X-ray diffraction set-up for dynamic compression experiments in the diamond anvil cell

Rachel J. Husband, a* Cornelius Strohm, Karen Appel, Orianna B. Ball, C Richard Briggs, d Johannes Buchen, Valerio Cerantola, Stella Chariton, f Amy L. Coleman, Hyunchae Cynn, Dana Dattelbaum, Anand Dwivedi, b Jon H. Eggert, d Lars Ehm, h William J. Evans, d Konstantin Glazyrin, a Alexander F. Goncharov, Heinz Graafsma, Alex Howard, Larissa Huston, Trevor Hutchinson, d Huijeong Hwang, Sony Jacob, Johannes Kaa, k,b Jaeyong Kim, Minseob Kim, Egor Koemets, Zuzana Konôpková, b Falko Langenhorst, Torsten Laurus, Xinyang Li, Iona Mainberger, Hauke Marquardt, Emma E. McBride, + Christopher McGuire, d James D. McHardy, Malcolm I. McMahon, R. Stewart McWilliams, Stewart McWilliams, Co. McHardy, Malcolm I. McMahon, Co. Stewart McWilliams, Co. McHardy, Co. McHard Alba S. J. Méndez, Anshuman Mondal, Guillaume Morard, Earl F. O'Bannon, d Christoph Otzen,^m Charles M. Pépin,^q Vitali B. Prakapenka,^f Clemens Prescher,^r Thomas R. Preston, b Ronald Redmer, Michael Roeper, a Carmen Sanchez-Valle, o Dean Smith, *§ Raymond F. Smith, d Daniel Sneed, d Sergio Speziale, u Tobias Spitzbart, a Stephan Stern, and Blake T. Sturtevant, Iolanta Sztuk-Dambietz, b Peter Talkovski, a Nenad Velisavljevic, d Cara Vennari, d Zhongyan Wu, l Choong-Shik Yoo, Ulf Zastrau, Zsolt Jeneid and Hanns-Peter Liermanna*

^aDeutsches Elektronen-Synchrotron DESY, Notkestr. 85, 22607 Hamburg, Germany, ^bEuropean XFEL, Holzkoppel 4, 22869 Schenefeld, Germany, 'The School of Physics and Astronomy, Centre for Science at Extreme Conditions, and SUPA, University of Edinburgh, Peter Guthrie Tait Road, Edinburgh EH9 3FD, United Kingdom, dawrence Livermore National Laboratory, Physical and Life Science Directorate, Livermore, CA 94550, USA, eUniversity of Oxford, Department of Earth Sciences, South Parks Road, Oxford OX1 3AN, United Kingdom, ^fThe University of Chicago, Consortium for Advanced Radiation Sources, 5640 South Ellis Avenue Chicago, IL 60637, USA, ⁸Los Alamos National Laboratory, Shock and Detonation Physics (M-9), PO 1663, Los Alamos, NM 87545, USA, hDepartment of Geosciences, 255 Earth and Space Sciences Building (ESS), Stony Brook, NY 11794-2100, USA, ¹Carnegie Science, Earth and Planets Laboratory, 5241 Broad Branch Road, NW, Washington, DC 20015, USA, JWashington State University, Department of Chemistry and Institute for Shock Physics, Pullman, WA 99164, USA, *Technische Universität Dortmund, Fakultät Physik/DELTA, Maria-Goeppert-Mayer-Straße 2, 44227 Dortmund, Germany, ^IHanyang University, Department of Physics, 17 Haengdang Dong, Seongdong gu Seoul 133-791, Republic of Korea, ^mFriedrich-Schiller-Universität Jena, Institut für Geowissenschaften, Burgweg 11, 07749 Jena, Germany, ⁿSLAC National Accelerator Laboratory, 2575 Sand Hill Road, Menlo Park, CA 94025, USA, Westfälische Wilhelms-Universität Münster, Institut für Mineralogie, Corrensstraße 24, 48149 Münster, Germany, PUniv. Grenoble Alpes, Univ. Savoie Mont Blanc, CNRS, IRD, Univ. Gustave Eiffel, ISTerre, 38000 Grenoble, France, ^qCEA, DAM, DIF, 91297 Arpajon Cedex, France, ^rUniversité Paris-Saclay, CEA, Laboratoire Matière en Conditions Extrêmes, 91680 Bruvères-le-Châtel, France, Albert-Ludwigs University of Freiburg, Institute of Earth and Environmental Sciences, Hermann-Herder-Str. 5, D-79104 Freiburg, Germany, ^tUniversität Rostock, Institut für Physik, Albert-Einstein-Straße 23–24, 18059 Rostock, Germany, ^uArgonne National Laboratory, High Pressure Collaborative Access Team (HPCAT), X-ray Science Division (XSD), 9700 S. Cass Avenue, Lemont, IL 60439, USA, and VHelmholtz-Zentrum Potsdam – Deutsches GeoForschungsZentrum (GFZ), Department 3: Geochemie-Chemie und Physik der Geomaterialien, Telegrafenberg, 14473 Potsdam, Germany. *Correspondence e-mail: rachel.husband@desy.de, hanns-peter.liermann@desy.de

An experimental platform for dynamic diamond anvil cell (dDAC) research has been developed at the High Energy Density (HED) Instrument at the European X-ray Free Electron Laser (European XFEL). Advantage was taken of the high repetition rate of the European XFEL (up to 4.5 MHz) to collect pulse-resolved MHz X-ray diffraction data from samples as they are dynamically compressed at intermediate strain rates ($\leq 10^3 \, \text{s}^{-1}$), where up to 352 diffraction images can be collected from a single pulse train. The set-up employs piezo-driven dDACs capable of compressing samples in \geq 340 µs, compatible with the maximum length of the pulse train (550 µs). Results from rapid compression experiments on a wide range of sample systems with different X-ray scattering powers are presented. A maximum compression rate of 87 TPa s⁻¹ was observed during the fast compression of Au, while a strain rate of \sim 1100 s⁻¹ was achieved during the rapid compression of N₂ at 23 TPa s⁻¹.

1. Introduction

115

116

117

118

120

121

122

124

125

126

127

129

130

131

132

133

134

135

136

137

138

139

141

142

143

145

146

147

148

149

150

151

152

153

154

155

156

159

160

161

162

163

164

165

166

167

168

169

170

171

Many materials respond to extreme pressures in the gigapascal (GPa) to terapascal (TPa) regime by transforming to exotic new phases, where transitions may be accompanied by changes in electronic structure and/or chemical bonding (McMahon & Nelmes, 2006). High-pressure structural behaviour has traditionally been investigated using X-rays at static high pressures using a large volume press or diamond anvil cell (DAC) (McMahon, 2018), or under dynamic compression using gas guns or laser-driven compression (Wark et al., 2022). These techniques are associated with very different timescales and strain rates ($\dot{\varepsilon} = d\varepsilon/dt$, where $\varepsilon = \Delta V/V$), which can result in striking differences in determined phase diagrams (Gorman et al., 2018; Pépin et al., 2019; Coleman et al., 2019; McBride et al., 2019; Marshall et al., 2021). Samples are compressed over minutes or hours in static compression experiments $(\dot{\varepsilon} < 10^{-3} \,\mathrm{s}^{-1})$, whereas the duration of shock and ramp compression experiments ($\dot{\varepsilon} = 10^5 - 10^9 \,\mathrm{s}^{-1}$) ranges from nanoseconds (laser-driven) to microseconds (gas gun-driven). Kinetic effects associated with phase transformations can sometimes result in significant differences in the observed phase transition pressures and temperatures under dynamic and static pressure conditions (Gorman et al., 2018; Pépin et al., 2019; Coleman et al., 2019; Marshall et al., 2021). In extreme cases, equilibrium phases can be completely absent in shock compression experiments (Gorman et al., 2018; Pépin et al., 2019), or metastable structures can form (Gorman et al., 2018; Pépin et al., 2019; Coleman et al., 2019). Phase boundaries can also be influenced by the presence of significant shear stresses in shock and ramp compression experiments due to uniaxial compression (McBride et al., 2019), the influence of which cannot be decoupled from kinetic effects.

Understanding kinetic effects is important to reconcile discrepancies between static and dynamic phase diagrams – particularly if material properties determined from dynamic compression studies are used to provide constraints on planetary interior models (Kraus et al., 2017; Wicks et al., 2018; Duffy & Smith, 2019; Coppari et al., 2021; Kim et al., 2022). However, despite the interest in rate- and timescale-related phenomena, material behaviour at intermediate compression rates ($\dot{\varepsilon} = 10^{-3} - 10^3 \,\mathrm{s}^{-1}$) remains relatively unexplored. This regime is accessible using dynamic DAC drivers (dDACs) (Evans et al., 2007; Sinogeikin et al., 2015; Jenei et al., 2019; Yan et al., 2022), which utilize piezoelectric actuators to compress samples in timescales ranging from milliseconds to several minutes. The maximum achievable strain rate is determined by the minimum compression timescale (i.e. piezo rise time) and largest accessible pressure range (i.e. force generation), where the latest generation of dDAC drivers can compress samples to the upper pressure limit of the diamond anvils in ~ 1 ms. For example, strain rates up to 500 s⁻¹ were generated during the fast compression of Au in 2.5 ms, which corresponds to the maximum compression rate (160 TPa s⁻¹) reported to date (Jenei et al., 2019). The dDAC also offers the additional advantage in that compression can either be performed hydrostatically through the use of a pressuretransmitting medium (PTM) or non-hydrostatically (without a PTM); the influence of the strain rate and stress state can therefore be decoupled.

172

173

174

175

176

177

178

179

180

181

182

183

184

185

186

187

189

190

191

192

193

194

195

196

197

198

199

200

201

202

203

204

205

206

207

208

209

210

211

212

213

214

215

216

217

218

219

220

221

222

223

224

225

226

227

228

Unlike conventional dynamic compression platforms where compression is inherently accompanied by high-temperature generation, dDAC compression does not necessarily lead to an increase in the sample temperature. The ability to compress along an isotherm means that dDAC experiments enable the exploration of well defined regions of pressure-temperature (P-T) space which are inaccessible using shock or ramp compression techniques, making it suitable for equation-ofstate (EoS) measurements in which the P-T path must be well known. Although the temperatures generated in shockless ramp compression (i.e. quasi-isentropic) are low enough for solid phases to be studied beyond 1 TPa (Fratanduono et al., 2020, 2021; Gorman et al., 2023) - significantly cooler than the shock Hugoniot - compression is not isothermal, and temperature determination can be very challenging as temperatures are often too low to measure with conventional streaked pyrometry (Gregor et al., 2016).

Investigation of material behaviour during dDAC compression requires appropriate time-resolved diagnostics which are compatible with the compression timescale. The development of high-frame-rate photon-counting X-ray detectors such as the LAMBDA (Pennicard et al., 2013) and the EIGER has permitted time-resolved X-ray diffraction (XRD) studies of dDAC-compressed samples to be performed at synchrotron radiation sources (Marquardt et al., 2018; Méndez et al., 2021, 2022; Husband, O'Bannon et al., 2021; Schoelmerich et al., 2022; O'Bannon et al., 2022), where high-Z sensors enable efficient detection of high-energy photons which are essential to penetrate the diamond anvils (≥10 keV) and provide sufficient access to reciprocal space for XRD experiments. However, minimum exposure times of \sim 500 μ s have in practice limited kinetic studies to compression rates of $\sim 1 \text{ TPa s}^{-1} \ (\dot{\varepsilon} \simeq 10^{-1} \text{ s}^{-1})$ – two orders of magnitude slower than achievable with the dDAC - in order for phase transition boundaries to be determined to within ~0.25 GPa (Husband, O'Bannon et al., 2021; O'Bannon et al., 2022). Under faster compression rates, the change in the sample pressure within each detector exposure (i.e. the pressure resolution) is too large to accurately pinpoint phase boundaries. For example, the pressure resolution is limited to ~40 GPa at the maximum reported compression rate (160 TPa s⁻¹) with current detector technology, whereas 3 µs exposure times would be required for a resolution of ~ 0.5 GPa. Although the next generation of photon-counting detectors promises about a tenfold increase in collection rate, this is still far from what is required to utilize the full dDAC capabilities. Synchrotron experiments are further limited by the available flux, where high-frame-rate data collection is limited to mid- or high-Z materials (Husband, O'Bannon et al., 2021, 2022) as low-Z materials require much longer exposure times [e.g. \sim 100 ms for H₂O (Méndez et al., 2021) and \sim 1 s for Li (Frost et al., 2019)].

The ability to collect meaningful data at strain rates above $\dot{\varepsilon} \sim 10^{-1} \, \mathrm{s}^{-1}$ requires access to faster X-ray diagnostics such

287

288

289

290

291

292

293

295

296

297

298

299

300

301

302

303

304

305

306

307

308

310

311

312

314

315

316

317

318

319

320

321

322

323

324

325

326

327

329

330

331

332

333

334

335

336

337

338

339

340

341

342

as those available at the European XFEL. The unique time structure of the European XFEL, in which a series of intense, ultrashort-timescale (<50 fs) X-ray pulses are produced at repetition rates up to 4.5 MHz, offers the potential to study material behaviour in a \leq 550 µs time window. This pulse train length is well suited to compression timescales achievable with current dDAC technology (\geq 340 µs), and the spacing between pulses (222 ns, 444 ns, 888 ns, etc.) provides the required time resolution to pinpoint phase boundaries within ~ 0.1 GPa. The European XFEL bunch structure has previously been used to study DAC compressed samples under dynamic temperature conditions using the DAC platform in interaction chamber 2 (IC2) (Liermann et al., 2021) at the High Energy Density (HED) instrument (Zastrau et al., 2021), where sequential X-ray pulses were used to probe the high-temperature state induced by the previous pulse in a pump-probe fashion (Meza-Galvez et al., 2020; Liermann et al., 2021; Hwang et al., 2021). However, these experiments did not have access to pulse-resolved XRD capabilities, but consecutive diffraction patterns of the pulse train were accumulated in a single image.

229

230

231

234

236

237

239

240

241

242

243

244

245

246

247

248

249

250

251

252

253

256

257

259

260

261

262 263

264

265

266267

268

269

270

271

272

273

274

276

277

278

279

280

281

282

283

284

285

Here, we describe the integration of the latest generation of dDAC drivers into the DAC platform at the HED instrument. An Adaptive Gain Integrating Pixel Detector (AGIPD) (Allahgholi et al., 2019) is used to collect pulse-resolved XRD data from dDAC compressed samples at the intra-train repetition rate of the European XFEL, providing time-resolved structural information during compression/decompression of the sample. Results from the fast compression of gold (Au) are presented to illustrate how X-ray heating can be minimized even in high-Z systems, which is important for kinetic studies where the P-T path must be well constrained. We also discuss the results from a series of experiments on four different phase-transforming materials - bismuth (Bi), titanium (Ti), nitrogen (N_2) and water (H_2O) – demonstrating the suitability of this platform for the study of a wide range of materials, from high- and mid-Z metallic systems to low-Z molecular solids. These data were collected as part of a DAC community proposal (#2592, by Liermann & Jenei), and are examples of the first dDAC compression experiments performed at the European XFEL.

2. Experimental platform

The following section describes the integration of two different types of dDAC drivers (Section 2.1) in the DAC platform in IC2 at the HED instrument (Zastrau *et al.*, 2021; Liermann *et al.*, 2021). The set-up inside IC2 consists of three dDACs installed in a revolving sample exchanger alongside an optical microscope that is used for sample visualization and alignment (Section 2.2). Pulse-resolved XRD data are collected using an AGIPD detector positioned outside of IC2 behind an Al window (Section 2.3), and the relative timing between the dDAC compression and the XFEL pulse train is controlled by an electrical drive scheme (Section 2.4).

2.1. dDAC drivers

This set-up utilizes piezo-driven dDACs in which the sample pressure is increased by the force applied to the upstream side

of a conventional DAC by a piezoelectric transducer. The force is controlled by the application of a time-dependent voltage waveform to the piezo, defining the temporal response of the pressure profile experienced during the experiment. The installation described here is compatible with two different dDAC designs developed at Deutsches Elektronen-Synchrotron (DESY) and Lawrence Livermore National Laboratory (LLNL) (Jenei et al., 2019), specifically designed for high force generation (and consequently, high sample pressures) at short timescales. In both designs, the piezo and DAC are contained within an external metallic housing with a threaded cap to ensure good mechanical contact between the actuator and the DAC. The design of the metallic housing enables easy exchange of numerous pre-loaded, standard DACs with relatively few piezoelectric drivers; as such, they are suitable for experiments in which data will be collected from a large number of DACs. The angular aperture which is useable for X-ray diffraction is the same as for the standard DAC, which is dependent both on the DAC design and the diamond/seat combination used on the downstream side. The DESY dDAC is used in conjunction with symmetric, pistoncylinder type DACs offering a 69.8° X-ray opening angle when equipped with a standard diamond facing upstream and a Boehler Almax (BA) diamond with a 70° X-ray aperture facing downstream. The LLNL dDAC is compatible with LLNL-type DACs with a slotted opening proving 55/90° X-ray coverage on the downstream side (Jenei et al., 2013). The LLNL DACs are equipped with standard cut diamonds mounted on a tungsten carbide (WC) seat facing upstream and a cubic boron nitride (cBN) seat facing downstream, so that X-ray coverage is limited by the slot opening in the DAC. The LLNL dDACs are equipped with an HPSt 1000/35-25/80 piezo actuator (Piezosystems Jena GmbH) and the DESY design is equipped with a 64-107 actuator (a PI Ceramic GmbH), both of which have a maximum operating voltage of 1000 V. When used in combination with the RCV 1000/7 amplifier (Piezosystems Jena GmbH), this gives a minimum rise time (0-1000 V) of 1.2 ms for the DESY dDAC and 340 µs for the LLNL dDAC. Full details of are given by Jenei et al. (2019).

The cell response (the initiation of a systematic, measurable sample pressure variation versus applied voltage) depends on the pre-compression applied by the tightening of the threaded cap. Reproducible pre-compression is therefore important to ensure repeatable timing between the drive voltage and the XFEL probe. For this reason, the dDAC housings were modified from their original design to integrate an interface for a torque wrench. In the DESY design, this was achieved by machining a hexagonal stud interface to a size 24 mm socket directly into the cap, whereas for the LLNL design this was accomplished using a four-pin adapter which couples to four holes in the threaded cap and has a square interface in the middle of the plate to attach it to a torque wrench (Fig. 1).

2.2. Installation inside IC2

The dDAC set-up is installed and operated under vacuum in IC2. In this set-up, three dDAC drivers are mounted in a

Schematics showing the dedicated (a) LLNL and (b) DESY dDAC housings. In (a), the threaded cap can be tightened with a torque wrench via an adapter which is attached to the dDAC housing. In (b), a torque wrench $\underline{\mathbf{is}}$ coupled via a standard socket to the hexagonal stud. The high-voltage connector is mounted to the body of the dDAC by a connector holder. A short-circuit connector with a 10 k Ω discharge resistor is connected during transport and storage to avoid unwanted build-up of charge.

motorized, carousel-type revolver which sits on a kinematic mount on the sample stack of the DAC platform (Liermann *et al.*, 2021) (Fig. 2). Switching between different dDACs is performed by rotating the revolver, which reduces the time required for sample exchange (including the time required to vent and pump IC2). The three dDACs are mounted in an interchangeable insert specific to the two different dDAC designs (DESY and LLNL), which can be exchanged without removing the entire revolver assembly. The inserts also feature three additional positions for reference and alignment samples, which typically consist of a diffraction standard for detector calibration (*e.g.* LaB₆), a set of W round edges for focus characterization, and a YAG screen for visualization of the XFEL beam via X-ray fluorescence. When installed inside the chamber, the piezoelectric actuators of the three dDACs

are connected to a high-voltage switchbox via individual hermetic feedthroughs mounted on a CF-type flange, which allows for the amplifier output to be switched between different actuators at the switchbox (Section 2.3).

Alignment of samples to the X-ray beam is performed using an optical microscope (Navitar) equipped with a vacuum-compatible camera (modified Basler), which is installed downstream of the revolver (Fig. 2). The microscope assembly is equipped with its own set of motorized translation stages which are used to align the camera to the X-ray beam, where the vertical translation stage additionally enables the objective to be removed from the beam path during data collection. Sample alignment parallel and perpendicular to the X-ray beam is performed using the XYZ translation stages of the sample stack.

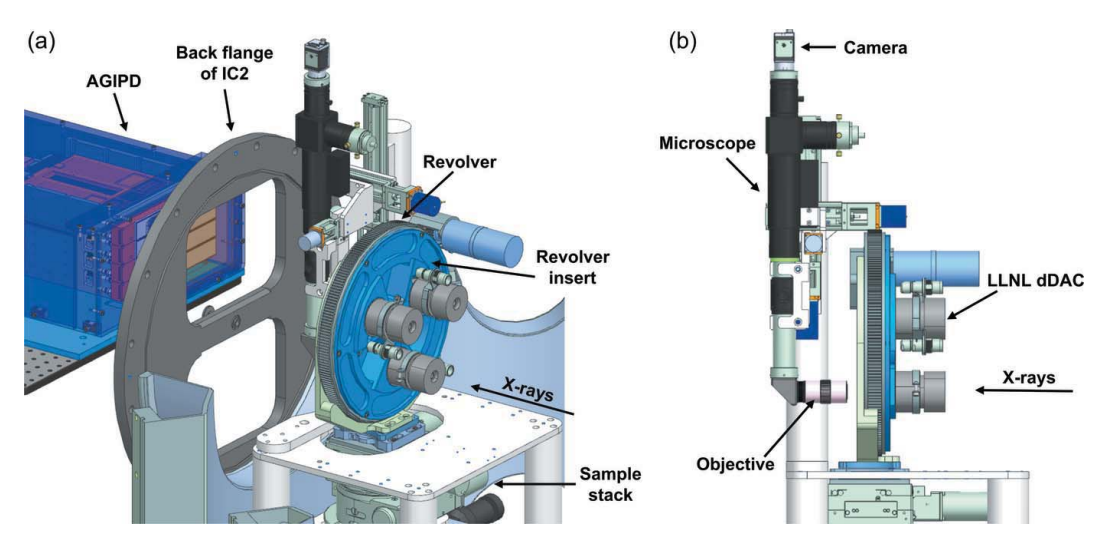


Figure 2
3D models showing two different viewpoints of the revolver and microscope installation inside IC2. Three LLNL-type dDACs are installed in the revolver insert. The microscope is shown in the X-ray beam path for viewing the sample.

515

516

517

518

519

520

521

523

524

525

526

527

528

529

530

531

532

533

534

535

536

537

538

539

540

541

542

543

544

545

546

547

548

549

550

551

552

553

554

555

556 557

558

559 560

561

562

563

564

565

566

567

568

569

570

2.3. AGIPD

457

458

459

460

461

462

464

466

467

468

469

470

471

472

473

474

475

476

477

478

479

480

481

483

484

485

487

488

489

490

491

492

493

494

495

496

497

498

500 501

502

504

505

506

507

508 509

510

511

512

513

A 500K AGIPD prototype (Allahgholi et al., 2019) is used to collect pulse-resolved XRD images during compression. The AGIPD is capable of collecting up to 352 images at the maximum intra-train repetition rate (up to 4.5 MHz) and read out at the train repetition rate (10 Hz), allowing for XRD data to be collected from consecutive pulse trains. The AGIPD 500K consists of eight 128×512 pixel modules with Si sensors (500 μ m thick) and a 200 μ m \times 200 μ m pixel size which are arranged in a 2×4 (horizontal \times vertical) configuration. Images collected when the pulse train is incident on the sample are subsequently extracted via the unique train ID. The AGIPD is positioned outside of IC2 on the detector bench, above the X-ray beam path. The detector bench allows for horizontal positioning of the AGIPD parallel and perpendicular to the X-ray beam. The back flange of IC2 is equipped with a 0.3 mm-thick Al window, which has \sim 71% transmission at 18.1 keV.

2.4. Electrical drive scheme

The piezoelectric actuators are controlled by an electrical drive scheme (Fig. 3) consisting of a waveform generator (Keysight 33522B), a high-voltage amplifier (HV-RCV 1000/7) and a high-voltage switch box designed in-house at DESY. The switch box commutates the amplifier output between three different piezoelectric actuators and a 20 µF internal capacitor, and prevents switching at high voltage to avoid the piezoelectric actuators remaining charged after they are disconnected from the amplifier. Piezoelectric actuators are short-circuited via a $10 \text{ k}\Omega$ discharge resistor when disconnected from the amplifier to avoid unwanted build-up of charge during storage, handling, pre-compression and loading into the revolver insert.

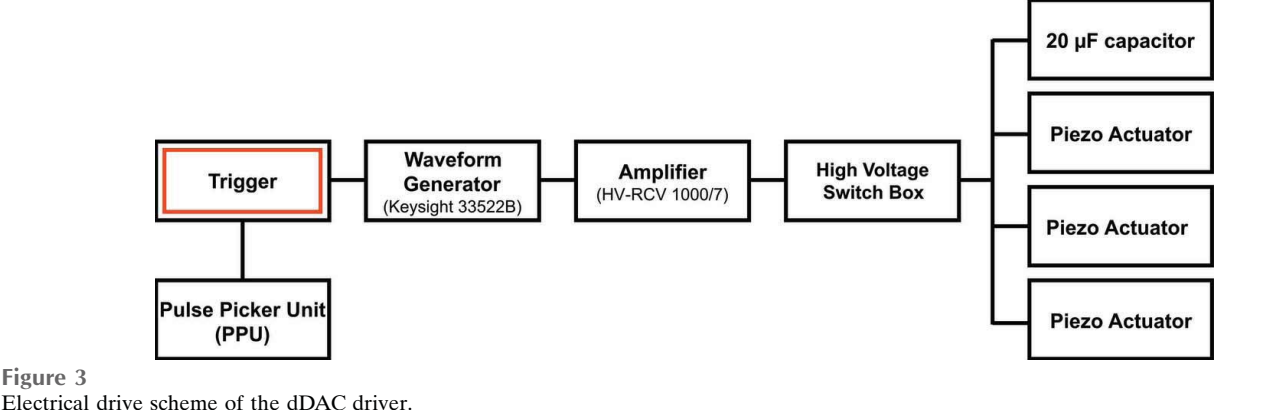
European XFEL provides pulse trains at a 10 Hz repetition rate, where each pulse train has a duration of $\leq 550 \,\mu s$ and an intra-train pulse repetition rate of 4.5/n MHz, where n is an integer (i.e. 2.2, 1.1, 0.5 MHz,...). Synchronization of the drive voltage and the X-ray trains is achieved using the XFEL timing system, which provides 10 Hz trigger signals synchronized to the XFEL trains. A deterministic scheme is used to trigger the waveform generator and pulse picker unit (PPU)

on a specific train ID, which allows for a single pulse train with a unique train ID to be transmitted to the sample. The trigger signal for the waveform generator has a local adjustable delay, so that data can be collected during different portions of the compression cycle. In the simplest mode of operation, timing of the voltage waveform is controlled by a single trigger signal (i.e. the waveform continues until completion) and data are collected using a single pulse train. Alternatively, the waveform can be defined in multiple segments which are triggered individually, so that data can be collected during several different sections of a compression cycle (e.g. during compression, hold and decompression). The experimental parameters can then be adjusted before the start of each individual segment such as the position of the sample in the XFEL beam (e.g. if the sample moved during compression), the X-ray intensity (i.e. beam attenuation) and the delay of the voltage waveform with respect to the start of the XFEL pulse train.

3. Dynamic compression experiments: experimental details

3.1. Overview

The capabilities of this platform are illustrated by experiments on five different sample systems (Table 1). Results from experiments on Au are first presented to illustrate the approach taken to minimize sample heating during data collection. This is followed by results from compression experiments on four different phase transforming materials: Bi, Ti, N₂ and H₂O. Experiments were designed to target one or two different phase transitions in each material, which are highlighted in their respective phase diagrams in Fig. 4. For each sample, an internal diffraction calibrant was added to the sample chamber for independent pressure determination. Previous work has shown that internal diffraction standards can be used for dDAC experiments on samples loaded with a PTM, provided that the sample/pressure marker assembly remains hydrostatic during compression (Husband, O'Bannon et al., 2021). However, in most of the runs described here, diffraction from the calibrant was unfortunately not observed



Details of the dynamic compression experiments described in this study.

The average pulse energy is corrected to account for absorption by the upstream diamond anvil using the attenuation length of diamond at 18.105 keV assuming the ambient pressure density of diamond (Henke *et al.*, 1993). The uncertainty in the average pulse energy corresponds to the standard deviation across the entire train.

Run No.	Sample details			X-ray parameters		Voltage waveform parameters			
	Sample	Pressure marker	PTM	X-ray transmission (%)	Energy/pulse on target (μJ)	dDAC assembly	Rise time (μs)	Maximum voltage (V)	Delay time (μs)
44	Au	W	Ne	0.3	0.2 ± 0.5	LLNL	340	1000	200
103	Bi	Cu	Ne	0.3	0.2 ± 0.4	LLNL	340	600	100
129	Ti	LiF, cBN	None	3	7 ± 3	DESY	960	800	760
140	N_2	LiF	N/A	75	220 ± 50	LLNL	340	1000	150
93	H_2O	cBN	N/A	25	60 ± 20	DESY	840	700	440

either because the diffracted signal was too weak or due to peak overlap with reflections from the sample or gasket.

Samples were screened at the Extreme Conditions Beamline (P02.2) (Liermann *et al.*, 2015) at the PETRA III synchrotron radiation source prior to the XFEL experiment to check the quality of the sample loading. Sample screening was performed before the DACs were loaded into the dDAC housing and a pre-torque was applied; consequently, the pressure determined during screening does not necessarily correspond to the starting pressure during the XFEL experiment.

3.2. XFEL parameters

The experiment was performed using a photon energy of 18.105 keV and an intra-train repetition rate of 1.1 MHz, which corresponds to an 888 ns spacing between XFEL pulses.

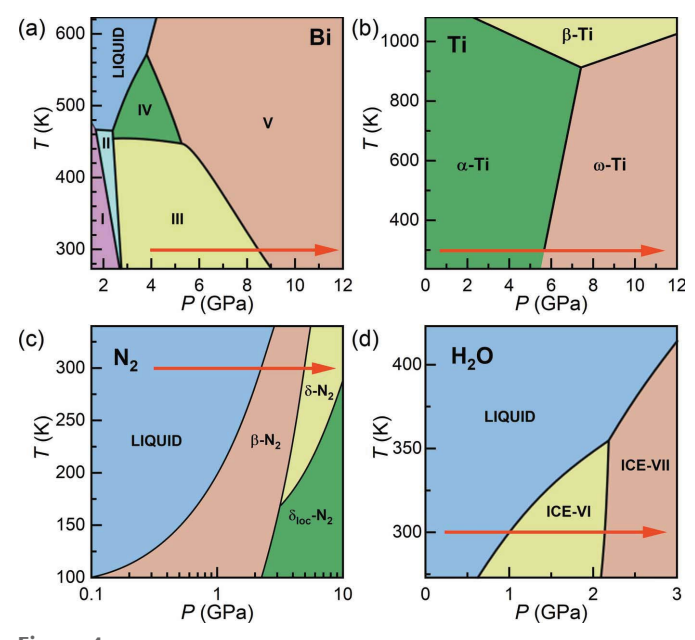


Figure 4
Phase diagrams of (a) Bi, (b) Ti, (c) N₂ and (d) H₂O, which are the phase transforming materials studied in this work. The red arrows show the ideal path taken during dDAC compression, highlighting the phase transitions targeted in these experiments. Phase diagrams are modified from the following references: Klement et al. (1963), Zhang et al. (2008a), Bini et al. (2000), Pistorius et al. (1968).

The X-ray beam was focused using a series of compound refractive lenses to a focal spot size of $\sim 50~\mu m$ (h) $\times 50~\mu m$ (v), which was determined from edge scans using a polished W rod. XRD data were collected using the AGIPD at the intratrain repetition rate of 1.1 MHz, which was chosen to maximize the data collection window based on the 352-image limit of the AGIPD. The pulse train length was limited to 191 μs in this experiment, which provided a total of 216 pulses per train. The sample-to-detector distance (SDD) and orientation of the AGIPD were calibrated using an LaB₆ NIST diffraction standard in conjunction with *DIOPTAS* software (Prescher & Prakapenka, 2015). The detector was positioned at an SDD of $\sim 480~mm$, which provided a *Q*-range coverage of 2.15–3.85 Å⁻¹. In this configuration, the *Q*-range coverage was limited by the size of the AGIPD.

The X-ray fluence was adjusted using a series of Si and diamond solid attenuators which determined the fraction of the XFEL beam which was transmitted to the sample (hereafter referred to as X-ray transmission and defined as a percentage of the unattenuated XFEL beam). The pulse energy was measured using a pulse-resolved intensity and position monitor (IPM) positioned upstream of the sample, which was cross-calibrated using an absolutely calibrated X-ray intensity gas monitor (XGM) before the start of the experiment. The pulse energy typically decreased over the course of the train, and the average pulse energy of each run is given in Table 1. All energies quoted in the remainder of the paper correspond to the energy at the sample position, corrected for absorption by the upstream diamond anvil using the attenuation length of diamond at 18.105 keV assuming ambient pressure density of diamond (Henke et al., 1993).

3.3. Sample alignment

High-pressure beamlines at synchrotron light sources typically use absorption scans to align samples to the X-ray beam and position them at the centre of a rotation axis defining the SDD. Scanning procedures are more time consuming at XFEL sources for several reasons: long count times due to the pulsed nature of the source; the need for pulse-to-pulse normalization due to pulse energy variations between different trains; and the need to use a heavily attenuated beam to avoid damage from repeated XFEL irradiation. Absorption scanning is

743

744

745

746

747

748

749

750

751

752

753

754

755

756

757

758

759

760

761

762

763

764

765

766

767

768

769

770

771

772

773

774

775

776

777

778

779

780

781

782

783

784

785

786

787

788

789

790

791

792

793

794

795

796

797

798

therefore typically reserved for essential alignment procedures where no other method is available.

Sample alignment was therefore performed using the optical microscope for the experiments described here. The microscope was aligned perpendicular to the X-ray beam based on the visual observation of X-ray induced fluorescence from a YAG screen at the sample position, after which the microscope was focused on the diffraction standard to define the sample plane (and SDD). Samples were then aligned to the focus of the optical microscope, which resulted in a \sim 1 mm offset in the SDD due to the high refractive index of the diamond anvil which was accounted for in the detector calibration.

3.4. Compression details

685

686

687

688

690

692

696

697

698

699

700

701

702

703

704

705

706

707

708

709

710

711

712

713

714

715

716

717

718

719

720

721

722

723

724

725

726

729

730

731

732

733

734

735

736

737

738

739

740

741

The cells were pre-compressed in the dDAC housing by applying a 5.0 (2.5) N m torque to the DESY (LLNL) dDAC assemblies prior to compression. Samples were compressed/ decompressed using a trapezoidal voltage waveform with the same rise, hold and fall times (Table 1) which was controlled by a single trigger, and data were collected during compression using a single \sim 191 μ s pulse train. The waveform was triggered before the start of the X-ray pulse train, and the delay time was chosen to target the pressure range of interest.

3.5. Diffraction data analysis

A total of 216 diffraction images were recorded for each run, which were radially integrated using DIOPTAS to produce 1D diffraction profiles from each frame. For runs performed using an X-ray transmission of >1%, the diffraction images were normalized to the IPM signal to account for intensity fluctuations of the incident beam energy during the pulse train prior to integration. This method of normalization was not possible for runs collected at lower X-ray transmissions because there was not sufficient signal on the IPM. The sample pressure was determined from the unit cell volume of the sample and/or pressure marker based on an EoS from the literature. With the exception of Bi-III, α -Ti and β -N₂, unit cell volumes were calculated from the position of the most intense diffraction peak, as other peaks were typically too weak for the peak position to be accurately determined. Although two reflections were clearly observed in Au, the unit cell volume was determined from the (111) reflection because it is least affected by uniaxial stress (Takemura & Dewaele, 2008). The compression rate was determined based on a linear fit to the pressure-time data in a selected time window (Δt) during which the pressure rise was approximately linear. The strain rate of the sample was calculated using $\dot{\varepsilon} = (V_2 - V_1)/(V_1 \Delta t)$, where V_1 and V_2 are the unit cell volumes of the sample at the start and end of the same time window (Δt), respectively.

4. Results

4.1. X-ray heating evaluation

Accurate knowledge of the P-T path is important in dynamic compression studies to discriminate how pressure and temperature affect phase transformation kinetics. XFEL experiments can be complicated by X-ray heating due to the high energy density of pulses. Unwanted X-ray heating is particularly problematic for high-Z materials, as X-ray absorption is roughly proportional to Z^4 (Meza-Galvez et al., 2020), which can potentially produce extreme temperatures in high-Z samples even when they are placed between conductive diamond anvils (Husband, McWilliams et al., 2021). Although XFEL heating could potentially be used to perform dDAC studies at high temperatures, these experiments face the challenge of independent pressure and temperature determination. Furthermore, irradiation with sequential pulses from the pulse train does not provide uniform heating, but produces temperature gradients in the irradiated (and probed) area and a sawtooth-type temperature-time profile (Meza-Galvez et al., 2020). For this reason, this work aimed to minimize heating in order to compress samples effectively isothermally room temperature.

X-ray heating can be minimized by reducing the total pulse energy, or by using a larger X-ray focal spot size to reduce the peak fluence. Increasing the beam size has the advantage that it minimizes the loss in diffracted intensity by increasing the illuminated sample volume (to the limit of the sample size), in contrast to higher attenuation which reduces the signal-tonoise ratio of the diffracted signal. A larger beam size also provides an improved powder average, which can be favourable for samples which show preferred orientation or larger crystallite sizes, especially due to the limited azimuthal coverage offered by the AGIPD. These experiments were therefore performed using an X-ray focal spot size of $\sim 50 \mu m$ FWHM, which was found to be a compromise between minimization of X-ray heating and parasitic diffraction and gasket heating originating from the tails of the beam. Internal pressure standards were chosen to have a smaller X-ray absorption coefficient (longer attenuation length, λ) than the sample to avoid unwanted heating of the pressure marker.

In order to evaluate the extent of X-ray heating to be expected during the dDAC experiment, the maximum allowable X-ray fluence for data collection was evaluated for each sample prior to the actual dynamic compression. This procedure is illustrated here for Au (Fig. 5), a high-Z element (Z =79) that is highly absorbing with $\lambda = 5.24 \,\mu\text{m}$ at 18.105 keV (Henke et al., 1993). Au is of particular interest for DAC experiments because it is chemically inert, does not undergo any structural transitions in the pressure range accessible in DAC compression experiments, and has a well calibrated thermobaric EoS in this pressure range (Anderson et al., 1989). For this reason, it is commonly used as an internal diffraction standard for pressure determination. Due to the differing sensitivities of X-ray heating ($\sim Z^4$) and diffraction intensity ($\sim Z^2$) to sample Z, Au represents a scenario for maximum heating in these experiments.

The Au sample was prepared in an LLNL-type DAC equipped with standard cut diamonds with 300 µm culets. Discs of 5 µm-thick Au foil and 3 µm-thick W foil were loaded into a stainless steel gasket with a 150 µm-diameter hole, and Ne was used as a PTM. XRD data collected at P02.2 indicated

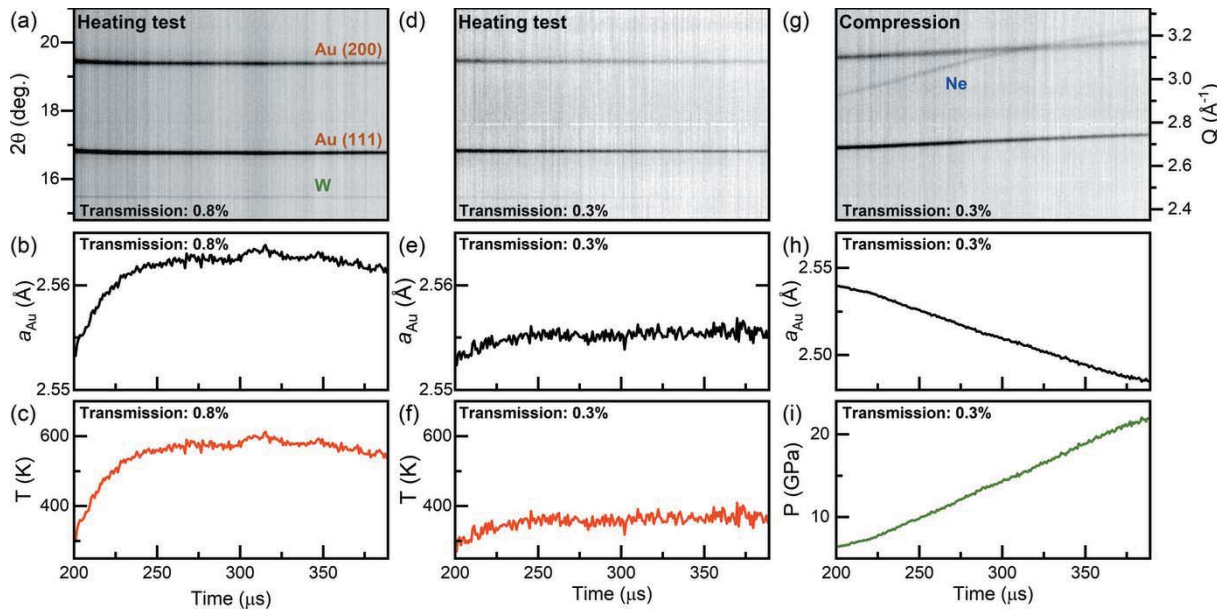


Figure 5 (a, d, g) Integrated XRD data collected from a sample of Au and Ne, illustrating the experimental procedure followed during a typical dDAC experiment. First, a heating test is performed at a given X-ray transmission (here 0.8%) to assess the extent of X-ray heating without compressing the sample [panels (a)–(c)]. If the temperature increase is too large, the heating test is repeated at a lower X-ray transmission [panels (a)–(f) at 0.3%] until the temperature rise is deemed acceptable for the experiment. Data are then collected using an appropriate X-ray transmission (here 0.3%) as the sample is compressed [panel (g)], and the pressure is determined based on the unit cell volume of the sample or pressure marker [panels (h) and (i)]. Pressure and temperature are determined assuming (c, f) isobaric and (i) isothermal conditions using the EoS of Au (Anderson $et\ al.$, 1989).

the initial pressure to be 0.9 GPa using the EoS of Au (Anderson *et al.*, 1989) and 1.2 GPa using the EoS of W (Dewaele *et al.*, 2004).

A series of 216 XRD images were collected at 1.1 MHz at a given X-ray transmission (here $0.8\% = 2 \pm 1 \mu J$) without compressing the sample to evaluate heating (Fig. 5). The starting pressure was estimated to be 3.3 GPa from the Au EoS, which is below the solidification pressure of Ne (Klotz et al., 2009). The \sim 2 GPa pressure increase from that measured at P02.2 is most likely due to the pre-torque applied to the DAC. The temperature increase was determined from the thermal expansion of the Au (Anderson et al., 1989) assuming the pressure remained constant throughout the run. If sample heating of >50 K was detected, the test was successively repeated at a lower X-ray transmission until an appropriate transmission was found (here 0.3%, below the detection limit of the IPM of 0.5 μJ). Only then were XRD data collected during dynamic compression. In both of the examples described here (0.8 and 0.3% transmission), the width of the (111) Au reflection remained constant throughout the run, suggesting the absence of temperature gradients within the probed sample volume.

The Au sample was compressed using the LLNL dDAC with a 340 μ s rise time up to 1000 V. XRD patterns were collected beginning 200 μ s after the start of the voltage ramp, providing data coverage during the last 140 μ s of the voltage rise and \sim 50 μ s of the plateau (Fig. 5). The pressure increase was limited to \sim 3 GPa in the first 200 μ s of the voltage ramp (before the start of XRD data collection), most likely related to a number of factors: the response of the dDAC assembly; the reproducibility of the amplifier response at such short rise

times; and the volume drop associated with Ne solidification. Ne lines were visible in the initial XRD patterns collected during the ramp, confirming that crystallization had occurred during the first 200 μs of the voltage rise. The pressure increase was approximately linear across the 191 μs X-ray window with an average compression rate of 87 TPa s $^{-1}$ ($\dot{\epsilon}=330~s^{-1}$), which was the highest compression rate achieved in this set of experiments. The 888 ns temporal resolution provided a pressure resolution of better than 0.1 GPa per frame at this compression rate, which is more than sufficient for kinetic studies.

4.2. Science case 1: dynamic compression of Bi

Bi is a high-Z (83), strongly scattering material which adopts numerous high-pressure polymorphs at relatively low P-T conditions. As such, it has been the focus of numerous laser-induced compression experiments which found significant deviations from the equilibrium phase diagram (Smith et al., 2008; Gorman et al., 2018; Pépin et al., 2019). Previous dDAC studies also reported rate-dependent behaviour (Yang et al., 2019; Husband, O'Bannon et al., 2021), where the Bi-III/ B-V phase boundary was observed to shift to higher pressures by as much as 2.5 GPa at ~ 1 TPa s⁻¹ (Husband, O'Bannon et al., 2021). Studies under faster compression rates were limited both by the available flux at synchrotron radiation sources and the maximum effective detector frame rate (4 kHz), which prevented the accurate determination of phase transition boundaries under faster compression rates. The time resolution of the European XFEL therefore offers the opportunity to extend these studies under faster compression rates.

The Bi sample was prepared in a LLNL-type DAC equipped with diamonds with 300 μ m culets. A \sim 35 μ m-diameter disk of 5 μ m-thick Bi foil was loaded into a 30 μ m-thick, 150 μ m-diameter sample chamber in a stainless steel gasket, and a 5 μ m-thick Cu disk was added as an internal diffraction standard. The Cu disk was spatially separated from the Bi foil to avoid unwanted chemical reactions that could be induced by X-ray heating. Ne was used as a PTM, and a small ruby sphere was added to the sample chamber for pressure determination after the loading process (Mao *et al.*, 1986). XRD data collected at P02.2 determined the pressure to be 1.5 GPa based on the unit cell volume of Cu (Dewaele *et al.*, 2004), and diffraction from the Bi foil showed the sample to be in the Bi-I phase (Degtyareva *et al.*, 2004).

A series of 216 XFEL diffraction images collected at 0.3% X-ray transmission (0.6 \pm 0.4 μ J) prior to compression showed no evidence of heating in Cu, which determined a pressure of 4.3 GPa using the EoS from Dewaele et al. (2004). This pressure is lower than the Ne solidification pressure, and in the stability field of Bi-III. Although Bi-III has a large number of diffraction lines, only two were observed due to preferred orientation of the crystal grains. The spotty nature of the Bi-III diffraction patterns is consistent with observations in previous dDAC experiments on both powder and foil samples (Husband, O'Bannon et al., 2021). Slight heating of Bi was observed in the first $\sim 25 \,\mu s$, with the Bi-III host lattice expanding by $\sim 0.4\%$. The azimuthal intensity distribution of the Bi-III diffraction spots was observed to remain constant across all XRD images, ruling out the possibility that the sample had melted and recrystallized after probing and subsequent thermalization in the 888 ns between consecutive XFEL pulses.

Bi was compressed using the LLNL dDAC with a 340 μs rise time up to 600 V. The Bi-III/Bi-V phase transition was clearly observed in XRD data collected using 0.3% X-ray transmission (0.2 \pm 0.4 μJ) (Fig. 6), where data collection started 100 μs after the start of the voltage waveform. The sample pressure was unchanged at the start of data collection, indicating a $\sim\!100~\mu s$ pressure response time for the dDAC assembly. This slow response may be related to the solidification of Ne at $\sim\!4.8$ GPa. The pressure was therefore determined from the Cu (111) peak position in the sum of six consecutive diffraction images.

The number of observed Bi-III reflections was insufficient to determine the unit cell volume. However, a rough pressure estimate was obtained from a linear fit to the (2110) peak position based on lattice parameters reported in previous work (Degtyareva *et al.*, 2004), which determined a starting pressure of \sim 4.3 GPa and a pressure of \sim 8.3 GPa for the first observation of Bi-V. No evidence of the high-temperature Bi-IV phase was observed, suggesting that the temperature remained below \sim 450 K (Klement *et al.*, 1963). The azimuthal position of the Bi-III reflections remained constant during compression, which again ruled out the possibility of melting and recrystallization between consecutive pulses.

Evidence of Bi-V was first observed 235 μ s after the start of the voltage waveform, where the pressure was estimated to be

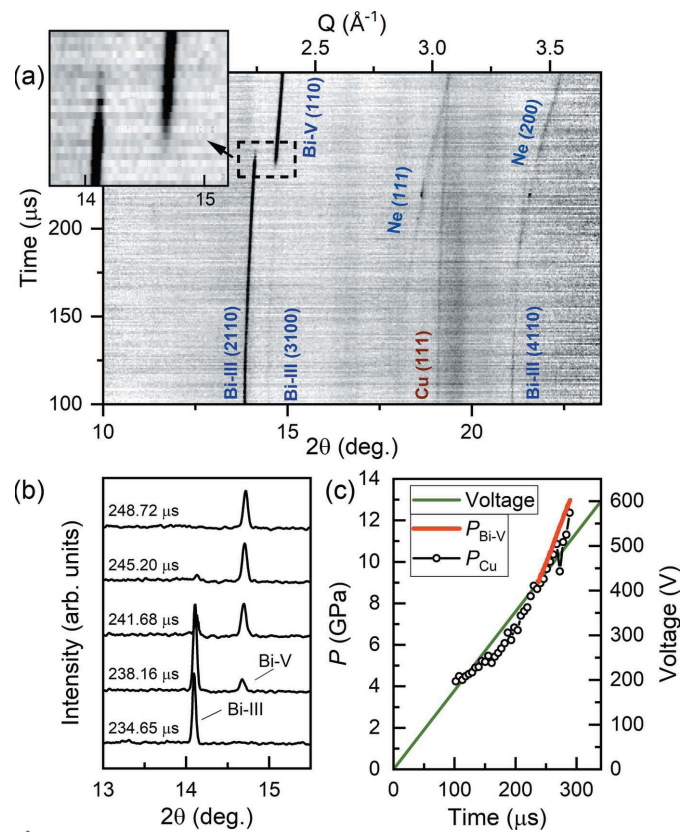


Figure 6 Dynamic compression of Bi. (a) Integrated XRD data as a function of time. (b) Selected integrated patterns illustrating the pressure-induced Bi-III/Bi-V structural phase transition. (c) Voltage applied to the piezo actuator and sample pressure as a function of time. In (a), the reflections from Bi-III, which has a host–guest structure, are identified using four Miller indices (hklm) (McMahon et al., 2007). In (c), $P_{\rm Bi}$ was determined using the EoS of Bi-V (Degtyareva et al., 2004) and $P_{\rm Cu}$ was determined using the EoS of Cu (Dewaele et al., 2004). The intensity of the Cu (111) reflection was very weak, and so $P_{\rm Cu}$ was determined from the sum of six consecutive diffraction images.

9.1 GPa based on the EoS of Bi-V (Degtyareva et al., 2004). The azimuthal intensity distribution of Debye-Scherrer rings from Bi-V was much more uniform than for Bi-III, which is more favourable for identifying the onset of the phase transition. A total of 13 mixed-phase Bi-III/Bi-V diffraction patterns were observed [Fig. 6(b)], indicating a timescale of \geq 11.4 µs for the transformation of the sample volume. The pressure increase was approximately linear in the Bi-V phase [Fig. 6(c)] with a compression rate of 76 TPa s⁻¹ – two orders of magnitude faster than previous work (Husband, O'Bannon et al., 2021) – which corresponds to a strain rate of 710 s⁻¹ in Bi-V. The observed transition pressure is the same as previously observed for Bi foils compressed at significantly lower compression rates ($\sim 10 \text{ GPa s}^{-1}$) (Husband, O'Bannon et al., 2021), which may be related to sample heating and the negative P-T slope of the Bi-III/Bi-V phase boundary.

4.3. Science case 2: dynamic compression of Ti

Ti (Z = 22) is an industrially and scientifically important metal due to its high strength-to-weight ratio and corrosion

resistance. Ti undergoes a martensitic structural transition from the hexagonal close-packed α -Ti phase to the hexagonal ω-Ti phase on compression at room temperature, where the onset transition pressure is dependent on multiple factors including material purity (Hennig et al., 2005), hydrostaticity (Errandonea et al., 2005) and compression rate (Tomasino & Yoo, 2017). Each of these factors, or combinations of them, can lead to a variation in the transition pressure from ~ 2 to 12 GPa. In particular, the presence of non-hydrostatic stress shifts the phase boundary to lower pressures (Errandonea et al., 2005), whereas compression rates > 74 GPa s⁻¹ shift it to higher pressures (Tomasino & Yoo, 2017). The transition is sluggish in all cases, and α - and ω -Ti coexist over a wide pressure range of 12 to ~17 GPa. The experiment described here was focused on the influence of compression rate on the α - ω phase transition pressure in Ti loaded without a PTM. This highlights the unique feature of the dDAC, which is that the stress state of the sample can be varied through the use (or absence) of a PTM.

A high-purity Ti sample [impurities (by weight): 360 parts per million (p.p.m.) O, 60 p.p.m. C, 10 p.p.m. N, 14 p.p.m. H, 4 p.p.m. Al, 3 p.p.m. V and 5 p.p.m. Fe (Velisavljevic *et al.*, 2014)] was loaded into a symmetric DAC equipped with 300 μ m culet diamonds. A stainless steel gasket with a 22 μ m-thick, 150 μ m-diameter gasket hole was used, and LiF and cBN were added to the sample chamber as internal pressure standards. Screening data collected at P02.2 confirmed that Ti was in the α -Ti phase, and the sample pressure was estimated to be 0.3 GPa based on cBN (Goncharov *et al.*, 2007) and 0 GPa based on Ti (Zhang *et al.*, 2008*b*). No diffraction signal from LiF was observed.

A series of 216 XFEL diffraction images collected at 3% X-ray transmission (7 \pm 3 μ J) prior to compression determined a pressure of 0.4 GPa from α -Ti. No LiF reflections were visible in the patterns but several intense, single-crystal-like reflections were observed from cBN, which corresponds to a pressure of 0.3 GPa (Goncharov *et al.*, 2007). The temperature increase during the run was estimated to be \sim 400 K based on the thermal expansion of cBN (Goncharov *et al.*, 2007) and \sim 220 K from Ti (Zhang *et al.*, 2008*b*).

The sample was compressed using the DESY dDAC with a 960 µs rise time up to 800 V, where XRD data were collected 760 µs after the start of the voltage waveform using 3% X-ray transmission (7 \pm 3 μ J) (Fig. 7). All reflections could be identified as originating from α -Ti, LiF, cBN or the gasket. Unfortunately, none of the LiF or cBN reflections were observed across the entire dataset, highlighting a potential issue when low-Z pressure markers are used to avoid X-ray heating; the (110) LiF reflection was obscured by the (0002) α -Ti reflection in all patterns, the (200) reflection overlapped with one of the gasket reflections at the start of data collection, and the (111) cBN reflection became too weak to be clearly identified at the end of data collection [Fig. 7(a)]. The pressure was therefore estimated from the unit cell volume of α -Ti (Errandonea et al., 2005). The sample pressure increased to 4.7 GPa in the first 760 μs (before the start of data collection), further increasing to 11.9 GPa at the end of the pulse train

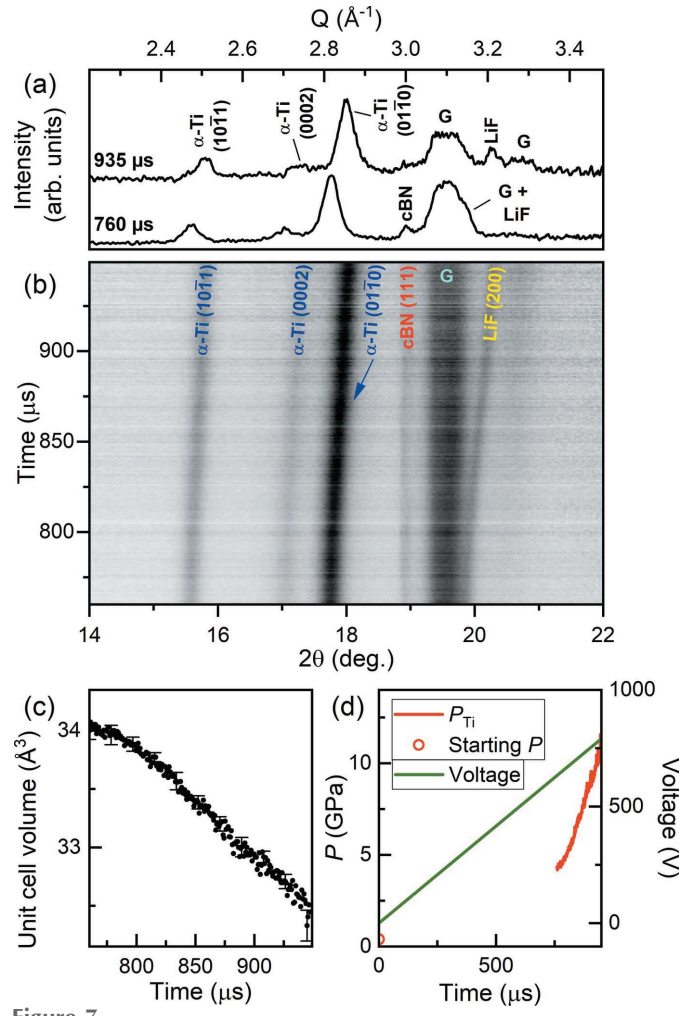


Figure 7 Dynamic compression of Ti. (a) Selected integrated diffraction patterns collected during the ramp, (b) integrated XRD data, (c) unit cell volume of α -Ti and (d) voltage applied to the piezo actuator and sample pressure as a function of time. In (a) and (b), **G** indicates reflections from the gasket. Error bars are shown for every 20th data point in (c).

with an average compression rate of 37 TPa s⁻¹ ($\dot{\varepsilon} = 240 \text{ s}^{-1}$ in α -Ti).

No evidence of ω -Ti was observed up to the highest pressure, which is >6 GPa above the α/ω equilibrium phase boundary at room temperature and >5.5 GPa at 520 K (Zhang et al., 2008a). An XRD map collected at the 16-ID-B beamline at HPCAT at the Advanced Photon Source in Argonne National Laboratory after the XFEL experiment found that the entire sample had fully transformed to ω -Ti and the pressure was estimated to be 21 GPa based on the ω -Ti EoS (Dewaele et al., 2015), which provides a lower bound on the maximum pressure reached during the compression. The absence of ω -Ti at \sim 12 GPa is surprising, as previous studies reported an onset transition pressure in samples loaded without a PTM ranging from 2-9 GPa [see Errandonea et al. (2005) and references therein]. However, the stress state of this sample is not well defined, as the limited 2θ coverage of the AGIPD prevents its determination using standard methods such as a line-shift analysis (Singh et al., 1998).

1199

1200

1201

1203

1204

1205

1206

1209

1210

1211

1213

1214

1215

1216

1217

1218

1219

1220

1221

1225

1226

1227

1228

1229

1230

1231

1232

1233

1234

1235

1236

1237

1239

1240

1241

1242

1243

1244

1245

1246

1247

1248

1249

1250

1251

1252

1253

1254

Further experiments are required to further constrain the extent of over-pressurization in Ti samples with a well defined stress state, shifting the X-ray window to higher pressures to also look at the phase coexistence region.

4.4. Science case 3: dynamic compression of N₂

1141

1142

1143

1144

1146

1147

1148

1149

1151

1152

1153

1154

1155

1156

1157

1158

1159

1160

1161

1162

1163

1164

1165

1166

1168

1169

1170

1171

1172

1173

1174

1175

1176

1178

1179

1180

1185

1186

1187

1188

1189

1190

1191

1192

1193

1194

1195

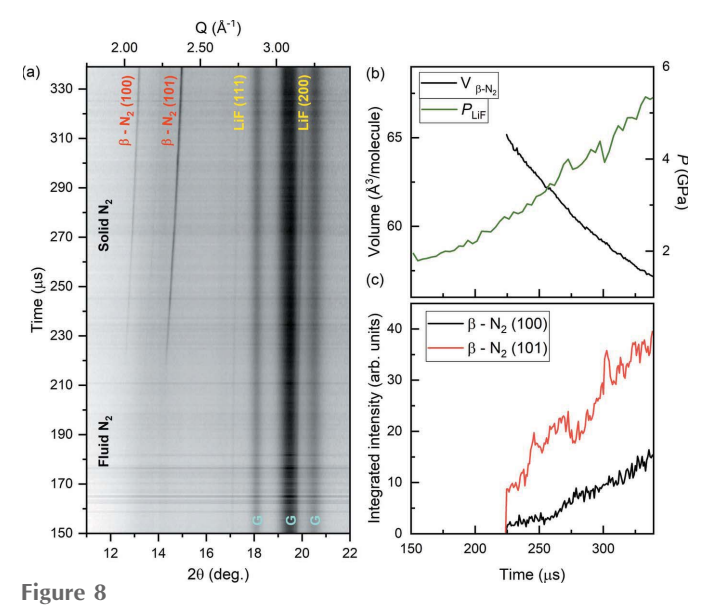
1196

1197

N₂ exhibits a striking degree of polymorphism at high pressures, adopting seven different solid molecular phases $(\alpha, \beta, \gamma, \delta, \delta^*, \varepsilon)$ and ζ) below 100 GPa. These phases are characterized by triple-bonded N₂ molecules and weak, intramolecular van der Waals bonding, with different degrees of lattice symmetry and orientational order. At higher pressures, structural changes are accompanied by changes in the chemical bonding such as transformations to amorphous (Gregoryanz et al., 2001) and polymeric (Eremets et al., 2004; Tomasino et al., 2014) structures which are associated with a large hysteresis (Eremets et al., 2001) and metastability (Gregoryanz et al., 2001). The ability to collect time-resolved XRD of fast compressed N₂ therefore offers the unique opportunity to study the structural evolution and phase transition kinetics in molecular solids at low pressures, and the compression-rate dependence of molecular to non-molecular transitions at higher pressures. The compression experiment described here focused on the low-pressure behaviour, specifically the pressure-induced solidification of N_2 .

The N₂ sample was loaded into an LLNL-type DAC equipped with diamonds with 500 µm culets. The DAC was prepared using a stainless steel gasket with a 30–40 µm-thick, 150 µm-diameter sample chamber, and a small grain of LiF was added as an internal diffraction standard. A small ruby sphere was added to the sample chamber to determine the pressure after loading (Mao et al., 1986). XRD data collected at P02.2 determined a pressure of 1.5 GPa based on the EoS of LiF (Dong et al., 2014), and diffuse scattering from liquid N₂ was clearly visible in the integrated diffraction patterns.

A series of 216 XRD images collected at 75% X-ray transmission (220 \pm 60 μ J) resulted in a <60 K temperature increase in LiF (Liu et al., 2007), which was deemed acceptable for this experiment. The LiF reflections were very weak, and so their peak position was determined from the sum of four diffraction images. N2 was compressed in the LLNL dDAC using a 340 µs rise time to 1000 V, and XRD data were collected 150 µs after the start of the voltage waveform. Solidification of N₂ was clearly observable in the XRD patterns [Fig. 8(a)], where β -N₂ reflections were present from 223.92 µs until the end of the XRD series. The EoS of LiF determined a solidification pressure of 2.7 GPa, which is 0.3 GPa higher than that observed in static compression studies (Zinn et al., 1987). An average compression rate of 20 TPa s⁻¹ across the entire X-ray window was determined based on the EoS of LiF. The compression rate was 23 TPa s⁻¹ in the region where β -N₂ was observed, corresponding to a strain rate of $\dot{\varepsilon} = 1100 \text{ s}^{-1}$ in β -N₂. N₂ remained in the β -N₂ phase up to at least 5.35 GPa, which is 0.35 GPa higher than the expected transition pressure to δ -N₂ (Hanfland *et al.*,



Dynamic compression of N₂. (a) Integrated XRD data, (b) sample pressure and molecular volume of N_2 , and (c) integrated intensity of β - N_2 reflections as a function of time. In (a), solidification of N_2 can be observed at \sim 220 μ s, and **G** indicates gasket peaks.

1998). Further experiments are required to determine the extent of over-pressurization of the β -N₂/ δ -N₂ transition.

4.5. Science case 4: dynamic compression of H₂O

H₂O has a complex phase diagram with 17 experimentally observed polymorphs, including two forms of amorphous ice at low temperatures and superionic ice at high temperatures (Millot et al., 2018, 2019; Queyroux et al., 2020; Prakapenka et al., 2021; Weck et al., 2022). On compression at room temperature, H₂O crystallizes in the ice-VI structure at 1.05 GPa (Shimizu et al., 1996), transforming to ice-VII at 2.1 GPa (Shimizu et al., 1996). The ice-VI melting curve has a positive P-T slope, terminating at the liquid/ice-VI/ice-VII triple point at 2.2 GPa and 354.75 K (Pistorius et al., 1968).

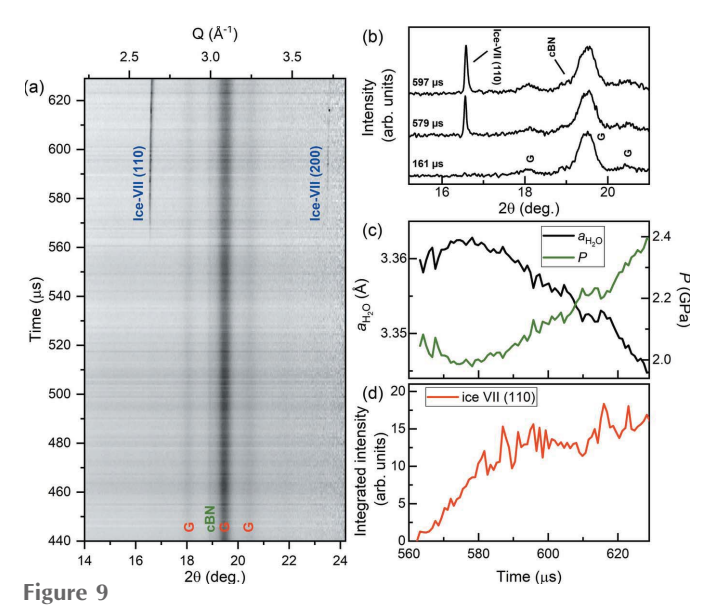
Laser-driven compression experiments reported striking deviations from the equilibrium phase diagram when H₂O is compressed along the quasi-isentrope (Dolan et al., 2007; Gleason et al., 2017; Marshall et al., 2021), which crosses the liquid/ice-VII phase boundary at 2.2 GPa (Myint et al., 2017). Shockless ramp-compression experiments found that liquid H₂O can be super-compressed to 8 GPa when compressed at 3×10^6 TPa s⁻¹ (Marshall et al., 2021), well into the stability field of ice-VII. This is currently thought to represent the metastability limit of liquid H₂O, where freezing is dominated by homogeneous nucleation (Marshall et al., 2021). H₂O has also been the focus of numerous dDAC studies which found that crystallization behaviour is highly dependent on compression rate: liquid H₂O crystallizes directly in ice-VI on slow compression, but transforms directly to either ice-VII or amorphous ice on fast compression (Lee et al., 2006; Chen & Yoo, 2011). Here, we focus on the pressure-induced crystallization of water at fast compression rates, providing direct structural identification using XRD which was not possible in earlier studies.

The H_2O sample was loaded into a symmetric DAC equipped with 500 μ m culet diamonds and a stainless steel gasket with a 39 μ m-thick sample chamber with a 250 μ m-diameter hole. A small grain of cBN was added to the sample chamber as an internal pressure standard, which was chosen due to its low X-ray absorption [λ = 5889 μ m (Henke *et al.*, 1993)] at this photon energy. A small ruby sphere was included for pressure determination after loading (Mao *et al.*, 1986). No ice reflections were observed in the XRD patterns collected at P02.2, and the presence of liquid H_2O was confirmed by the observation of a diffuse scattering signal. The pressure was estimated to be 0 GPa based on the EoS of cBN (Goncharov *et al.*, 2007), which was slightly lower than the pressure of 0.27 GPa estimated from the ruby.

X-ray heating of H_2O is a relatively minor issue because of its low X-ray absorption at 18.105~keV [$\lambda=7383~\mu\text{m}$ at 1~GPa (Henke *et al.*, 1993)], allowing for data to be collected with a relatively high X-ray fluence. No ice reflections were observed in the series of 216 diffraction images collected at 25% X-ray transmission ($60~\pm~20~\mu\text{J}$) prior to compression, suggesting that the sample was still in the liquid phase. This was confirmed by the observation of a weak diffuse scattering signal from liquid in the integrated diffraction patterns. Heating of H_2O could not be assessed due to the absence of ice reflections. A pressure of 1.3 GPa was determined from cBN (Goncharov *et al.*, 2007), which is above the H_2O solidification pressure. However, this could be related to the high bulk modulus of cBN, which makes it insensitive to small pressure changes.

The sample was compressed using an 840 µs rise time up to 700 V, and XRD data were collected 440 µs after the start of the voltage waveform using 25% X-ray transmission (60 \pm 20 μJ) (Fig. 9). No ice reflections were observed during the first 125 µs of data collection, suggesting that H₂O was still in the liquid phase. No evidence of ice-VI was observed during compression; instead, the sample transformed directly from liquid to ice-VII. Accurate determination of the pressure from cBN was prevented due to its partial overlap with the gasket peaks [Fig. 9(b)]. However, ice-VII indicated a crystallization pressure of 2.1 GPa (Klotz et al., 2017), which is identical to the ice-VI/ice-VII equilibrium transition pressure at ambient temperature. The pressure remained approximately constant for $\sim 20 \,\mu s$ after the first observation of ice-VII [Fig. 9(c)], which is most likely related to the volume drop associated with the liquid/ice-VII transition and the time taken for the entire sample to transform. This is supported by the simultaneous increase in the integrated intensity of the (110) ice-VII reflection [Fig. 9(d)]. A linear pressure increase was observed after the pressure plateau, which corresponds to a compression rate of 8.1 TPa s⁻¹ and a strain rate of $\dot{\varepsilon} = 350 \text{ s}^{-1}$ in ice-VII.

Our observation of the crystallization of ice-VII directly from super-compressed water is in good agreement with previous dDAC studies which used Raman and visual observation as phase identification methods (Lee *et al.*, 2006; Chen & Yoo, 2011), and is the first time in which this has been detected using XRD. However, we note that a temperature



Dynamic compression of H_2O . The panels show (a) integrated XRD data as a function of time, (b) selected integrated patterns showing the growth of the ice-VII reflection during compression, (c) the lattice parameter and corresponding pressure of ice-VII and (d) the integrated intensity of the (110) ice-VII reflection as a function of time. In (c), the pressure is determined using the EoS of ice-VII (Klotz et al., 2017). In (a) and (b), G indicates reflections from the gasket.

increase of just ~ 50 K is sufficient to bypass the ice-VI phase on compression [Fig. 4(d)], which cannot be ruled out in this work. Further experiments are therefore required to decouple temperature- and rate-induced transition pathways in high-pressure $\rm H_2O$.

5. Outlook

The dDAC platform at the HED instrument was successfully commissioned as part of DAC community proposal #2592 (Liermann and Jenei), which demonstrated that this set-up can be used to collect time-resolved XRD data from a wide range of materials as they are dynamically compressed using piezodriven dDACs. The ability to collect XRD data at the intratrain repetition rate of the European XFEL (1.1 MHz) provided a temporal resolution of 888 ns, which corresponds to a pressure resolution of <0.1 GPa per frame at the compression rates accessed in this study (up to 87 TPa s⁻¹). This section describes future developments which will extend the capabilities of this set-up to a provide a more versatile platform.

Several upgrades are anticipated for the dDAC platform. A planned update of the high-voltage amplifier will provide higher currents up to 20 A, leading to shorter rise times and faster compression rates. This will be used in conjunction with the DESY dDAC, which has a rise time longer than the maximum pulse train length in the current configuration. In addition, IC2 was designed to accommodate a 1 megapixel (1M) AGIPD protruding into the vacuum chamber, which would significantly improve the *Q*-range and coverage due to the smaller SDD and increased detector area. Development is ongoing and implementation is planned for the near future.

1427

1428

1429

1430

1431

1432

1433

1434

1435

1436

1437

1438

1439

1440

1441

1442

1443

1444

1445

1446

1447

1448

1449

1450

1451

1452

1453

1454

1455

1456

1457

1458

1459

1460

1461

1462

1463

1464

1465

1466

1467

1468

1469

1470

1471

1472

1473

1474

1475

1476

1477

1478

1479

1480

1481

1482

There is also an ongoing development program of a high-Zversion of the AGIPD 1M, which is designed for higher photon energies. From the facility side, European XFEL is capable of providing the HED instrument with photon energies up to 25 keV. Moving to higher photon energies offers two major advantages for dDAC experiments. First, X-ray heating is reduced because samples have a lower X-ray absorbance. Second, higher energies increase access to reciprocal space, which is fundamentally limited by photon energy due to the limited opening angle of the DAC. The combination of higher X-ray energies with larger detectors such as the AGIPD 1M has the potential to extend dDAC experiments to pair distribution function studies of liquid or amorphous materials.

The experiments described here were performed using a \sim 200 µs pulse train; the standard configuration offered by European XFEL where the 600 µs pulse train is split between the three undulators (SASE 1-3). In this operation mode, the delay time between the XFEL and the dDAC voltage waveform must be carefully chosen to align the X-ray window with the pressure range of interest. European XFEL has recently implemented a 'long pulse train' mode in which every nth train is delivered only to SASE 2. This mode was commissioned with n = 100 and a 550 µs pulse train, where timing between the dDAC and the 'long' train can be performed using the methods described here. In this case, a total of 310 AGIPD images can be collected using a reduced intra-train repetition rate of 0.56 MHz, providing data coverage over the entire length of the pulse train.

6. Conclusion

1369

1370

1371

1374

1376

1377

1379

1380

1381

1382

1383

1384

1385

1386

1387

1388

1390

1391

1392

1393

1394

1396

1397 1398

1400

1401

1402

1403

1404

1405

1406

1407

1408

1409

1410

1411

1412

1413

1414

1415

1416

1417

1418

1419

1420

1421

1422

1423

1424

1425

This work describes an experimental set-up at the HED instrument at the European X-ray Free Electron Laser which is capable of collecting pulse-resolved XRD data from samples as they are dynamically compressed using piezodriven diamond anvil cells. Compression timescales of ≥340 µs are perfectly suited to the pulse train length (200– 550 μs), where the use of the AGIPD provides pulse-resolved XRD data at the intra-train repetition rate of the XFEL source. The capabilities of this platform are demonstrated by results from experiments on a range of different material systems with different X-ray absorption lengths. A maximum compression rate of ~ 87 TPa s⁻¹ was achieved during the fast compression of Au, and a maximum strain rate of $\sim 1100 \text{ s}^{-1}$ was achieved during the compression of N_2 at 18 TPa s⁻¹. Varying the X-ray fluence and using a relatively large focal spot size limited X-ray heating even in the high-Z systems, demonstrating that this platform is suitable for kinetic studies in which the P-T path must be well constrained.

Acknowledgements

We acknowledge European XFEL in Schenefeld, Germany, for provision of X-ray free-electron laser beam time at Scientific Instrument HED (High Energy Density Science) and would like to thank the staff for their assistance. The authors are indebted to the HIBEF user consortium for the provision of instrumentation and staff that enabled this experiment. We acknowledge DESY (Hamburg, Germany), a member of the Helmholtz Association HGF, for the provision of experimental facilities. Parts of this research were carried out at PETRA III (beamline P02.2). We thank MW (DESY) for his help with the design of the electrical wiring scheme. A portion of this work was performed at HPCAT (Sector 16), Advanced Photon Source (APS), Argonne National Laboratory. HPCAT operations are supported by DOE-NNSA's Office of Experimental Sciences. The Advanced Photon Source is a US Department of Energy (DOE) Office of Science User Facility operated for the DOE Office of Science by Argonne National Laboratory under Contract No. DE-AC02-06CH1135.

Funding information

The following funding is acknowledged: Lawrence Livermore National Laboratory (grant No. DE-AC52-07NA27344); H2020 European Research Council (grant No. 864877 to Hauke Marquardt); U.S. Department of Energy, National Nuclear Security Administration (grant No. DE-NA-0004091 to Choong-Shik Yoo); National Science Foundation (grant No. DMR 2112653 to Choong-Shik Yoo); UK Research and Innovation (award No. MR/W008211/1 to Emma E. McBride); Deutsche Forschungsgemeinschaft (grant No. SA 2585/5-1 to Rachel J. Husband, Hanns-Peter Liermann, Anshuman Mondal, Carmen Sanchez-Valle); Alexander von Humboldt-Stiftung (award to Huijeong Hwang).

References

Allahgholi, A., Becker, J., Delfs, A., Dinapoli, R., Goettlicher, P., Greiffenberg, D., Henrich, B., Hirsemann, H., Kuhn, M., Klanner, R., Klyuev, A., Krueger, H., Lange, S., Laurus, T., Marras, A., Mezza, D., Mozzanica, A., Niemann, M., Poehlsen, J., Schwandt, J., Sheviakov, I., Shi, X., Smoljanin, S., Steffen, L., Sztuk-Dambietz, J., Trunk, U., Xia, Q., Zeribi, M., Zhang, J., Zimmer, M., Schmitt, B. & Graafsma, H. (2019). J. Synchrotron Rad. 26, 74-82.

Anderson, O. L., Isaak, D. G. & Yamamoto, S. (1989). J. Appl. Phys. **65**, 1534–1543.

Bini, R., Ulivi, L., Kreutz, J. & Jodl, H. J. (2000). J. Chem. Phys. 112, 8522-8529.

Chen, J.-Y. & Yoo, C.-S. (2011). Proc. Natl Acad. Sci. 108, 7685–7688. Coleman, A. L., Gorman, M. G., Briggs, R., McWilliams, R. S., McGonegle, D., Bolme, C. A., Gleason, A. E., Fratanduono, D. E., Smith, R. F., Galtier, E., Lee, H. J., Nagler, B., Granados, E., Collins, G. W., Eggert, J. H., Wark, J. S. & McMahon, M. I. (2019). Phys. Rev. Lett. 122, 255704.

Coppari, F., Smith, R. F., Wang, J., Millot, M., Kim, D., Rygg, J. R., Hamel, S., Eggert, J. H. & Duffy, T. S. (2021). Nat. Geosci. 14, 121-126.

Degtyareva, O., MCMahon, M. I. & Nelmes, R. J. (2004). High. Press. Res. 24, 319-356.

Dewaele, A., Loubeyre, P. & Mezouar, M. (2004). Phys. Rev. B, 70, 094112.

Dewaele, A., Stutzmann, V., Bouchet, J., Bottin, F., Occelli, F. & Mezouar, M. (2015). Phys. Rev. B, 91, 134108.

Dolan, D. H., Knudson, M. D., Hall, C. A. & Deeney, C. (2007). Nat. Phys. 3, 339-342.

Dong, H., Dorfman, S. M., Holl, C. M., Meng, Y., Prakapenka, V. B., He, D. & Duffy, T. S. (2014). High. Press. Res. 34, 39-48. Duffy, T. S. & Smith, R. F. (2019). Front. Earth Sci. 7, 23.

1486

1487

1488

1490

1491

1492

1493

1494

1495

1496

1497

1498

1499

1501

1502

1503

1504

1505

1506

1510

1512

1513

1514

1515

1516

1517

1518

1519

1521

1522

1527

1529

1530

1531

1532

1535

1536

1537

1539

- Eremets, M. I., Gavriliuk, A. G., Trojan, I. A., Dzivenko, D. A. & Boehler, R. (2004). *Nat. Mater.* **3**, 558–563.
 - Eremets, M. I., Hemley, R. J., Mao, H. & Gregoryanz, E. (2001). *Nature*, **411**, 170–174.
 - Errandonea, D., Meng, Y., Somayazulu, M. & Häusermann, D. (2005). *Physica B*, **355**, 116–125.
 - Evans, W. J., Yoo, C.-S., Lee, G. W., Cynn, H., Lipp, M. J. & Visbeck, K. (2007). Rev. Sci. Instrum. 78, 073904.
 - Fratanduono, D. E., Millot, M., Braun, D. G., Ali, S. J., Fernandez-Pañella, A., Seagle, C. T., Davis, J.-P., Brown, J. L., Akahama, Y., Kraus, R. G., Marshall, M. C., Smith, R. F., O'Bannon, E. F., McNaney, J. M. & Eggert, J. H. (2021). *Science*, **372**, 1063–1068.
 - Fratanduono, D. E., Smith, R. F., Ali, S. J., Braun, D. G., Fernandez-Pañella, A., Zhang, S., Kraus, R. G., Coppari, F., McNaney, J. M., Marshall, M. C., Kirch, L. E., Swift, D. C., Millot, M., Wicks, J. K. & Eggert, J. H. (2020). *Phys. Rev. Lett.* **124**, 015701.
 - Frost, M., Kim, J. B., McBride, E. E., Peterson, J. R., Smith, J. S., Sun, P. & Glenzer, S. H. (2019). *Phys. Rev. Lett.* **123**, 065701.
 - Gleason, A. E., Bolme, C. A., Galtier, E., Lee, H. J., Granados, E., Dolan, D. H., Seagle, C. T., Ao, T., Ali, S., Lazicki, A., Swift, D., Celliers, P. & Mao, W. L. (2017). *Phys. Rev. Lett.* **119**, 025701.
 - Goncharov, A. F., Crowhurst, J. C., Dewhurst, J. K., Sharma, S., Sanloup, C., Gregoryanz, E., Guignot, N. & Mezouar, M. (2007). Phys. Rev. B, 75, 224114.
 - Gorman, M. G., Coleman, A. L., Briggs, R., McWilliams, R. S., McGonegle, D., Bolme, C. A., Gleason, A. E., Galtier, E., Lee, H. J., Granados, E., Śliwa, M., Sanloup, C., Rothman, S., Fratanduono, D. E., Smith, R. F., Collins, G. W., Eggert, J. H., Wark, J. S. & McMahon, M. I. (2018). Sci. Rep. 8, 16927.
 - Gorman, M. G., Wu, C. J., Smith, R. F., Benedict, L. X., Prisbrey, C. J.,
 Schill, W., Bonev, S. A., Long, Z. C., Söderlind, P., Braun, D., Swift,
 D. C., Briggs, R., Volz, T. J., O'Bannon, E. F., Celliers, P. M.,
 Fratanduono, D. E., Eggert, J. H., Ali, S. J. & McNaney, J. M. (2023).
 Phys. Rev. B, 107, 014109.
 - Gregor, M. C., Boni, R., Sorce, A., Kendrick, J., McCoy, C. A., Polsin,
 D. N., Boehly, T. R., Celliers, P. M., Collins, G. W., Fratanduono,
 D. E., Eggert, J. H. & Millot, M. (2016). Rev. Sci. Instrum. 87, 114903.
 - Gregoryanz, E., Goncharov, A. F., Hemley, R. J. & Mao, H. (2001).
 Phys. Rev. B, 64, 052103.
 - Hanfland, M., Lorenzen, M., Wassilew-Reul, C. & Zontone, F. (1998). Rev. High Press. Sci. Technol. 7, 787–789.
 - Henke, B. L., Gullikson, E. M. & Davis, J. C. (1993). At. Data Nucl. Data Tables, 54, 181–342.
 - Hennig, R. G., Trinkle, D. R., Bouchet, J., Srinivasan, S. G., Albers, R. C. & Wilkins, J. W. (2005). *Nat. Mater.* 4, 129–133.
 - Husband, R. J., McWilliams, R. S., Pace, E. J., Coleman, A. L., Hwang,
 H., Choi, J., Kim, T., Hwang, G. C., Ball, O. B., Chun, S. H., Nam, D.,
 Kim, S., Cynn, H., Prakapenka, V. B., Shim, S.-H., Toleikis, S.,
 McMahon, M. I., Lee, Y. & Liermann, H.-P. (2021). Commun.
 Mater. 2. 61.
 - Husband, R. J., O'Bannon, E. F., Liermann, H.-P., Lipp, M. J., Méndez, A. S. J., Konôpková, Z., McBride, E. E., Evans, W. J. & Jenei, Z. (2021). Sci. Rep. 11, 14859.
 - Hwang, H., Kim, T., Cynn, H., Vogt, T., Husband, R. J., Appel, K., Baehtz, C., Ball, O. B., Baron, M. A., Briggs, R., Bykov, M., Bykova, E., Cerantola, V., Chantel, J., Coleman, A. L., Dattlebaum, D., Dresselhaus-Marais, L. E., Eggert, J. H., Ehm, L., Evans, W. J., Fiquet, G., Frost, M., Glazyrin, K., Goncharov, A. F., Jenei, Z., Kim, J., Konôpková, Z., Mainberger, J., Makita, M., Marquardt, H., McBride, E. E., McHardy, J. D., Merkel, S., Morard, G., O'Bannon, E. F., Otzen, C., Pace, E. J., Pelka, A., Pépin, C. M., Pigott, J. S., Prakapenka, V. B., Prescher, C., Redmer, R., Speziale, S., Spiekermann, G., Strohm, C., Sturtevant, B. T., Velisavljevic, N., Wilke, M., Yoo, C.-S., Zastrau, U., Liermann, H.-P., McMahon, M. I., McWilliams, R. S. & Lee, Y. (2021). J. Phys. Chem. Lett. 12, 3246–3252.

Jenei, Z., Cynn, H., Visbeck, K. & Evans, W. J. (2013). Rev. Sci. Instrum. 84, 095114.

1540

1541

1542

1543

1545

1546

1547

1548

1551

1554

1555

1556

1558

1559

1560

1561

1562

1563

1565

1567

1569

1570

1571

1573

1574

1575

1578

1579

1580

1581

1583

1584

1586

1587

1589

1590

1591

1592

1595

1596

- Jenei, Z., Liermann, H. P., Husband, R., Méndez, A. S. J., Pennicard, D., Marquardt, H., O'Bannon, E. F., Pakhomova, A., Konopkova, Z., Glazyrin, K., Wendt, M., Wenz, S., McBride, E. E., Morgenroth, W., Winkler, B., Rothkirch, A., Hanfland, M. & Evans, W. J. (2019). Rev. Sci. Instrum. 90, 065114.
- Kim, D., Smith, R. F., Ocampo, I. K., Coppari, F., Marshall, M. C., Ginnane, M. K., Wicks, J. K., Tracy, S. J., Millot, M., Lazicki, A., Rygg, J. R., Eggert, J. H. & Duffy, T. S. (2022). *Nat. Commun.* 13, 2260.
- Klement, W., Jayaraman, A. & Kennedy, G. C. (1963). *Phys. Rev.* **131**, 632–637.
- Klotz, S., Chervin, J.-C., Munsch, P. & Le Marchand, G. (2009). J. Phys. D Appl. Phys. 42, 075413.
- Klotz, S., Komatsu, K., Kagi, H., Kunc, K., Sano-Furukawa, A., Machida, S. & Hattori, T. (2017). Phys. Rev. B, 95, 174111.
- Kraus, D., Vorberger, J., Pak, A., Hartley, N. J., Fletcher, L. B., Frydrych, S., Galtier, E., Gamboa, E. J., Gericke, D. O., Glenzer, S. H., Granados, E., MacDonald, M. J., MacKinnon, A. J., McBride, E. E., Nam, I., Neumayer, P., Roth, M., Saunders, A. M., Schuster, A. K., Sun, P., van Driel, T., Döppner, T. & Falcone, R. W. (2017). Nat. Astron. 1, 606–611.
- Lee, G. W., Evans, W. J. & Yoo, C.-S. (2006). Phys. Rev. B, 74, 134112. Liermann, H. P., Konôpková, Z., Appel, K., Prescher, C., Schropp, A., Cerantola, V., Husband, R. J., McHardy, J. D., McMahon, M. I., McWilliams, R. S., Pépin, C. M., Mainberger, J., Roeper, M., Berghäuser, A., Damker, H., Talkovski, P., Foese, M., Kujala, N., Ball, O. B., Baron, M. A., Briggs, R., Bykov, M., Bykova, E., Chantel, J., Coleman, A. L., Cynn, H., Dattelbaum, D., Dresselhaus-Marais, L. E., Eggert, J. H., Ehm, L., Evans, W. J., Fiquet, G., Frost, M., Glazyrin, K., Goncharov, A. F., Hwang, H., Jenei, Z., Kim, J.-Y., Langenhorst, F., Lee, Y., Makita, M., Marquardt, H., McBride, E. E., Merkel, S., Morard, G., O'Bannon, E. F., Otzen, C., Pace, E. J., Pelka, A., Pigott, J. S., Prakapenka, V. B., Redmer, R., Sanchez-Valle, C., Schoelmerich, M., Speziale, S., Spiekermann, G., Sturtevant, B. T., Toleikis, S., Velisavljevic, N., Wilke, M., Yoo, C.-S., Baehtz, C., Zastrau, U. & Strohm, C. (2021). J. Synchrotron Rad. **28**. 688–706.
- Liermann, H.-P., Konôpková, Z., Morgenroth, W., Glazyrin, K., Bednarčik, J., McBride, E. E., Petitgirard, S., Delitz, J. T., Wendt, M., Bican, Y., Ehnes, A., Schwark, I., Rothkirch, A., Tischer, M., Heuer, J., Schulte-Schrepping, H., Kracht, T. & Franz, H. (2015). J. Synchrotron Rad. 22, 908–924.
- Liu, J., Dubrovinsky, L., Boffa Ballaran, T. & Crichton, W. (2007). High. Press. Res. 27, 483–489.
- Mao, H. K., Xu, J. & Bell, P. M. (1986). J. Geophys. Res. 91, 4673–4676.
- Marquardt, H., Buchen, J., Mendez, A. S. J., Kurnosov, A., Wendt, M., Rothkirch, A., Pennicard, D. & Liermann, H.-P. (2018). *Geophys. Res. Lett.* **45**, 6862–6868.
- Marshall, M. C., Millot, M., Fratanduono, D. E., Sterbentz, D. M., Myint, P. C., Belof, J. L., Kim, Y.-J., Coppari, F., Ali, S. J., Eggert, J. H., Smith, R. F. & McNaney, J. M. (2021). *Phys. Rev. Lett.* 127, 135701.
- McBride, E. E., Krygier, A., Ehnes, A., Galtier, E., Harmand, M., Konôpková, Z., Lee, H. J., Liermann, H.-P., Nagler, B., Pelka, A., Rödel, M., Schropp, A., Smith, R. F., Spindloe, C., Swift, D., Tavella, F., Toleikis, S., Tschentscher, T., Wark, J. S. & Higginbotham, A. (2019). *Nat. Phys.* **15**, 89–94.
- McMahon, M. I. (2018). Vol. Synchrotron Light Sources and Free-Electron Lasers: Accelerator Physics, Instrumentation and Science Applications, edited by E. Jaeschke, S. Khan, J. R. Schneider & J. B. Hastings, pp. 1–40. Cham: Springer International Publishing (https://doi.org/10.1007/978-3-319-04507-8_67-1).
- McMahon, M. I., Degtyareva, O., Nelmes, R. J., van Smaalen, S. & Palatinus, L. (2007). *Phys. Rev. B*, **75**, 184114.
- McMahon, M. I. & Nelmes, R. J. (2006). Chem. Soc. Rev. 35, 943–963.

1655

1656

1657

1659

1660

1661

1662

1665

1666

1667

1668

1669

1670

1672

1673

1674

1675

1676

1677

1678

1681

1683

1685

1686

1689

1690 1691

1692

1693

1696 1697

1699

1700

1701

1703

1704 1705

1706

1707

1708 1709

1710

Méndez, A. S. J., Stackhouse, S., Trautner, V., Wang, B., Satta, N., Kurnosov, A., Husband, R. J., Glazyrin, K., Liermann, H.-P. & Marquardt, H. (2022). J. Geophys. Res. Solid Earth, 127, e2021JB023832.

1597

1598

1602

1605

1607

1608

1609

1610

1611

1612

1613

1614

1615

1616

1617

1618

1619

1620

1624

1625

1626

1627

1628

1629

1630

1631

1632

1635

1636

1640

1642

1643

1644

1645 1646

1647

1649

1650

1651

1653

- Méndez, A. S. J., Trybel, F., Husband, R. J., Steinle-Neumann, G., Liermann, H.-P. & Marquardt, H. (2021). Phys. Rev. B, 103, 064104.
- Meza-Galvez, J., Gomez-Perez, N., Marshall, A. S., Coleman, A. L., Appel, K., Liermann, H. P., McMahon, M. I., Konôpková, Z. & McWilliams, R. S. (2020). J. Appl. Phys. 127, 195902.
- Millot, M., Coppari, F., Rygg, J. R., Correa Barrios, A., Hamel, S., Swift, D. C. & Eggert, J. H. (2019). Nature, 569, 251-255.
- Millot, M., Hamel, S., Rygg, J. R., Celliers, P. M., Collins, G. W., Coppari, F., Fratanduono, D. E., Jeanloz, R., Swift, D. C. & Eggert, J. H. (2018). Nat. Phys. 14, 297–302.
- Myint, P. C., Benedict, L. X. & Belof, J. L. (2017). J. Chem. Phys. 147, 084505.
- O'Bannon, E. F., Husband, R. J., Baer, B. J., Lipp, M. J., Liermann, H.-P., Evans, W. J. & Jenei, Z. (2022). Sci. Rep. 12, 17294.
- Pennicard, D., Lange, S., Smoljanin, S., Hirsemann, H., Graafsma, H., Epple, M., Zuvic, M., Lampert, M.-O., Fritzsch, T. & Rothermund, M. (2013). J. Phys. Conf. Ser. 425, 062010.
- Pépin, C. M., Sollier, A., Marizy, A., Occelli, F., Sander, M., Torchio, R. & Loubeyre, P. (2019). Phys. Rev. B, 100, 060101.
- Pistorius, C. W. F. T., Rapoport, E. & Clark, J. B. (1968). J. Chem. Phys. 48, 5509-5514.
- Prakapenka, V. B., Holtgrewe, N., Lobanov, S. S. & Goncharov, A. F. (2021). Nat. Phys. 17, 1233-1238.
- Prescher, C. & Prakapenka, V. B. (2015). High. Press. Res. 35, 223-
- Queyroux, J.-A., Hernandez, J.-A., Weck, G., Ninet, S., Plisson, T., Klotz, S., Garbarino, G., Guignot, N., Mezouar, M., Hanfland, M., Itié, J.-P. & Datchi, F. (2020). Phys. Rev. Lett. 125, 195501.
- Schoelmerich, M. O., Mendez, A. S. J., Plueckthun, C., Biedermann, N., Husband, R., Preston, T. R., Wollenweber, L., Klimm, K., Tschentscher, T., Redmer, R., Liermann, H. P. & Appel, K. (2022). Phys. Rev. B, 105, 064109.
- Shimizu, H., Nabetani, T., Nishiba, T. & Sasaki, S. (1996). Phys. Rev. B, **53**, 6107–6110.
- Singh, A. K., Balasingh, C., Mao, H., Hemley, R. J. & Shu, J. (1998). J. Appl. Phys. 83, 7567–7575.

- Sinogeikin, S. V., Smith, J. S., Rod, E., Lin, C., Kenney-Benson, C. & Shen, G. (2015). Rev. Sci. Instrum. 86, 072209.
- Smith, R. F., Eggert, J. H., Saculla, M. D., Jankowski, A. F., Bastea, M., Hicks, D. G. & Collins, G. W. (2008). Phys. Rev. Lett. 101, 065701. Takemura, K. & Dewaele, A. (2008). Phys. Rev. B, 78, 104119.
- Tomasino, D., Kim, M., Smith, J. & Yoo, C.-S. (2014). Phys. Rev. Lett. **113**, 205502.
- Tomasino, D. & Yoo, C.-S. (2017). AIP Conf. Proc. 1793, 060002.
- Velisavljevic, N., Jacobsen, M. K. & Vohra, Y. K. (2014). Mater. Res. Expr. 1, 035044.
- Wark, J. S., McMahon, M. I. & Eggert, J. H. (2022). J. Appl. Phys. 132,
- Weck, G., Queyroux, J.-A., Ninet, S., Datchi, F., Mezouar, M. & Loubeyre, P. (2022). Phys. Rev. Lett. 128, 165701.
- Wicks, J. K., Smith, R. F., Fratanduono, D. E., Coppari, F., Kraus, R. G., Newman, M. G., Rygg, J. R., Eggert, J. H. & Duffy, T. S. (2018). Sci. Adv. 4, eaao5864.
- Yan, J., Liu, X., Gorelli, F. A., Xu, H., Zhang, H., Hu, H., Gregoryanz, E. & Dalladay-Simpson, P. (2022). Rev. Sci. Instrum. 93, 063901.
- Yang, D.-L., Liu, J., Lin, C.-L., Jing, Q.-M., Zhang, Y., Gong, Y., Li, Y.-C. & Li, X.-D. (2019). Chin. Phys. B, 28, 036201.
- Zastrau, U., Appel, K., Baehtz, C., Baehr, O., Batchelor, L., Berghäuser, A., Banjafar, M., Brambrink, E., Cerantola, V., Cowan, T. E., Damker, H., Dietrich, S., Di Dio Cafiso, S., Dreyer, J., Engel, H.-O., Feldmann, T., Findeisen, S., Foese, M., Fulla-Marsa, D., Göde, S., Hassan, M., Hauser, J., Herrmannsdörfer, T., Höppner, H., Kaa, J., Kaever, P., Knöfel, K., Konôpková, Z., Laso García, A., Liermann, H.-P., Mainberger, J., Makita, M., Martens, E.-C., McBride, E. E., Möller, D., Nakatsutsumi, M., Pelka, A., Plueckthun, C., Prescher, C., Preston, T. R., Röper, M., Schmidt, A., Seidel, W., Schwinkendorf, J.-P., Schoelmerich, M. O., Schramm, U., Schropp, A., Strohm, C., Sukharnikov, K., Talkovski, P., Thorpe, I., Toncian, M., Toncian, T., Wollenweber, L., Yamamoto, Sh. & Tschentscher, T. (2021). J. Synchrotron Rad. 28, 1393–1416.
- Zhang, J., Zhao, Y., Hixson, R. S., Gray, G. T., Wang, L., Utsumi, W., Hiroyuki, S. & Takanori, H. (2008a). J. Phys. Chem. Solids, 69, 2559-2563.
- Zhang, J., Zhao, Y., Hixson, R. S., Gray, G. T., Wang, L., Utsumi, W., Hiroyuki, S. & Takanori, H. (2008b). Phys. Rev. B, 78, 054119.
- Zinn, A. S., Schiferl, D. & Nicol, M. F. (1987). J. Chem. Phys. 87, 1267–1271.



ISSN: 1600-5775

YOU WILL AUTOMATICALLY BE SENT DETAILS OF HOW TO DOWNLOAD AN ELECTRONIC REPRINT OF YOUR PAPER, FREE OF CHARGE. PRINTED REPRINTS MAY BE PURCHASED USING THIS FORM.

Please scan your order and send to tw@iucr.org	
INTERNATIONAL UNION OF CRYSTALLOGRAPHY 5 Abbey Square Chester CH1 2HU, England.	Article No.: S230391-FV5162
VAT No. GB 161 9034 76	
Title of article A MHz X-ray diffraction set-up for dynamic compression	experiments in the diamond anvil cell
Name Rachel J. Husband	
Address Deutches Elektronen-Synchrotron (DESY), Notkestr. 85, Hamburg	, 22607, Germany
E-mail address (for electronic reprints) rachel.husband@desy.de	
OPEN ACCESS	
Journal of Synchrotron Radiation is an open access journal.	
DIGITAL PRINTED REPRINTS	
I wish to order paid reprints	
These reprints will be sent to the address given above. If the above	re address or e-mail address is not correct, please indicate an alternative:
PAYMENT	
Charge for reprints USD	
An official purchase order made out to INTERNATIONAL UNIC	N OF CRYSTALLOGRAPHY is enclosed will follow
Purchase order No.	
Please invoice me	
I wish to pay by credit card	
EU authors only: VAT No:	
	1
Date	Signature

DIGITAL PRINTED REPRINTS

An electronic reprint is supplied free of charge.

Printed reprints without limit of number may be purchased at the prices given in the table below. The requirements of all joint authors, if any, and of their laboratories should be included in a single order, specifically ordered on the form overleaf. All orders for reprints must be submitted promptly.

Prices for reprints are given below in **United States dollars** and include postage.

	Size of paper (in printed pages)					
Number of reprints required	1–2	3–4	5–8	9–16	Additional 8's	
50	184	268	372	560	246	
100	278	402	556	842	370	
150	368	534	740	1122	490	
200	456	664	920	1400	610	
Additional 50's	86	128	178	276	116	

PAYMENT AND ORDERING

Official purchase orders should be made out to INTERNATIONAL UNION OF CRYSTALLOGRAPHY.

Orders should be returned by email to tw@iucr.org

ENQUIRIES

Enquiries concerning reprints should be sent to support@iucr.org.